

MARINE ENERGY HARVESTING FROM LOW CUT-IN
SPEEDS HORIZONTAL AXIS OCEAN CURRENT TURBINE:
DESIGN, OPTIMIZATION AND ANALYSIS OF THE ROTOR

REZA CHINI



Marine Energy Harvesting from Low Cut-in Speeds Horizontal
Axis Ocean Current Turbine: Design, Optimization and Analysis
of the Rotor

By

© Reza Chini

A thesis submitted to the
School of Graduate Studies
In partial fulfillment of the
Requirements for the degree of
Master of Engineering

Department of Engineering and Applied Science
Memorial University of Newfoundland

June 2012
St. John's, Newfoundland, Canada

Abstract

Energy extraction from tidal currents using marine current turbines has been gaining attention in recent years. In the first part of this thesis, the design and optimization of a horizontal axis turbine is proposed to harvest available ocean kinetic energy from very low speed flow regimes. A horizontal axis marine current turbine is modeled and NACA 4 series foils are selected as the two-dimensional blade foils design domain. Blade geometry and foil shape are then optimized using Response Surface (RSM) and Steepest Ascent Methodologies (SAM). The performance and accuracy of the proposed design is compared and validated with the developed turbine Blade Element Momentum (BEM) theory model. In the second part of the thesis, hydrodynamic properties of the optimized foil are simulated through a commercial Computational Fluid Dynamic (CFD) package and then compared with the conventional Eppler 61 foil properties. The two-dimensional analysis confirms the effectiveness of the optimization for the Reynolds number of 42000. A three dimensional start-up *CFD* simulation is then performed to calculate the unsteady load distribution over the blade surfaces which have been further utilized in a static Finite Element Analysis (FEA) to measure the rotor's blade tip deflection. This stage guarantees the safe and optimum structural performance of the rotor in regard to various existing material choices and manufacturing technologies.

Acknowledgements

First I would like to express my appreciation to my supervisors Dr. Martin Ordonez and Dr. Ralf Bachmayer for their valuable guidance, knowledge and patience during my master's program.

The financial support of this research has been provided by National Science Engineering Research Council of Canada (NSERC) and School of Graduate Studies, Memorial University of Newfoundland and Labrador.

I would like to thank my fellow graduate students and officemates, Mr. Haibing Wang, Mr. Zhi Li, Mr. Ming Xi, Mr. Brian Claus, Mr. Peng Wen, Mr. Khalid Hasan and Mr. Mahmud Hasan, who provided me with an enjoyable and peaceful atmosphere. Appreciation is extended to Dr. Syed Ahmad Imtiaz for his helpful discussions. I would like to also acknowledge my appreciation to Dr. Leonard Lye, the Associate Dean of Graduate Studies and Research and Ms. Moya Crocker, the Secretary to the Associate Dean. Finally, I would like to thank my former supervisor Dr. Seyed Ali Jazayeri and my dear friend Mr. Amir Ahmad Roohi for their guidance and consultancy throughout my master's program.

Table of Contents

Abstract	i
Acknowledgments	ii
Table of Contents	iii
List of Figures	vi
List of Tables	xi
Nomenclature	xiii
List of Appendices	xv
1 Introduction	1
1.1 Literature Review of Turbine Based Technology	9
1.1.1 Horizontal Axis Turbine Modelling Techniques	10
1.1.2 Rotor Optimization Techniques	11
1.1.3 Rotor Computational Fluid Dynamics and Finite Element Analysis	13
1.2 Thesis Objectives	14
1.3 Thesis Organization	15
2 Horizontal Axis Ocean Current Turbine (HAOT) Modelling	17
2.1 Blade Hydrodynamics Theory and Vortex System	18
2.1.1 Lift and Drag forces	19
2.1.2 Vortex System	20
2.1.3 Momentum Theory	23
2.1.4 Lift and Drag Coefficients	25
2.1.5 Blade Element Momentum Theory	27
2.2 BEM model Results and Validation	32

2.2.1 Blade Pitch Angle Effects.....	37
2.2.2 Blade's Length Effects	39
2.2.3 Number of Blade's Effects	41
2.2.4 Blade's Shape Effects.....	43
2.3 Low Flow Current Considerations	43
2.4 Summary	45
3 Blade Optimization Using Response Surface Methodology	48
3.1 Blade Optimization Descriptions	48
3.1.1 Blade Design Factors and Related Constraints	48
3.1.2 Statistical Modelling Strategies	50
3.1.3 Optimization Methodology	51
3.2 Full Factorial Exploratory Design.....	52
3.3 Response Surface Method Design.....	54
3.3.1 The First Exploratory Design (1 st Optimization Step).....	56
3.3.2 The Second Exploratory Design (1 st Optimization Step).....	64
3.3.3 The Third Exploratory Design (1 st Optimization Step).....	68
3.3.4 The First Exploratory Design (2 nd Optimization Step).....	72
3.3.5 The Second Exploratory Design (2 nd Optimization Step)	73
3.4 Optimization Validation.....	76
3.5 Optimization Discussion	77
3.6 Summary	80
4 Foil and Blade CFD Analysis	82
4.1 Two-Dimensional Analysis.....	82
4.1.1 Two-Dimensional Problem Definition and Parameters.....	83
4.1.2 Two-Dimensional Finite Volume Mesh.....	84
4.1.3 Time or Iteration Averaging	85
4.1.4 Eppler 61 Simulation Results.....	93
4.1.5 Eppler 61 Simulation Validation.....	98
4.1.6 NACA 6603 Simulation Results.....	98

4.2 Rotor Three-Dimensional (3D) Startup Considerations.....	105
4.2.1 Three-Dimensional Problem Definition and Parameters.....	107
4.2.2 Three-Dimensional Finite Volume Mesh.....	109
4.2.3 Three-Dimensional Blade Pressure Distribution.....	110
4.3 Finite Element Analysis of Blade Tip Deflection.....	115
4.3.1 Manufacturing Processes and Materials.....	115
4.3.2 Three Dimensional Finite Element Mesh.....	117
4.3.3 Blade Tip Deflection Analysis Results.....	118
4.4 Summary.....	125
5 Conclusions.....	127
5.1 Summary.....	127
5.2 Contributions.....	128
5.3 Future Work.....	131
References.....	133
Appendices.....	145
Appendix A.....	145
Appendix B.....	148
Appendix C.....	153

List of Figures

Fig. 2.1 Six bladed horizontal axis rotor.....	20
Fig. 2.2 Lift and drag visualization.....	20
Fig. 2.3 NACA 0015 lift coefficient vs. angle of attacks	21
Fig. 2.4 NACA 0015 drag coefficient vs. angle of attacks	21
Fig. 2.5 Geometric, effective and induced angle of attacks.....	22
Fig. 2.6 Axial and rotational velocities.....	23
Fig. 2.7 Control volumes around the rotor.....	24
Fig. 2.8 Power and thrust coefficients vs. axial induction factor.....	26
Fig. 2.9 NACA 0015 lift coefficient validations ($Re = 80000$).....	27
Fig. 2.10 NACA 0015 drag coefficient validations ($Re = 80000$).....	28
Fig. 2.11 Normal (F_N) and tangential (F_T) components of total force (R).....	29
Fig. 2.12 Blades twist angle distribution	33
Fig. 2.13 Blade thickness distribution.....	33
Fig. 2.14 Linear vs. Non-linear thickness blade distribution effect on rotor power	34
Fig. 2.15 Schematic of a three bladed rotor.....	36
Fig. 2.16 Power coefficient validation.....	36
Fig. 2.17 Rotor's power vs. rotor speed.....	37
Fig. 2.18 Power coefficient vs. blade's pitch angle ($V_0 = 1\text{m/s}$).....	38
Fig. 2.19 Extracted power vs. blade's pitch angle ($V_0 = 1\text{m/s}$).....	38
Fig. 2.20 Power coefficient vs. blade length.....	39
Fig. 2.21 Extracted power vs. blade length.....	40
Fig. 2.22 Power coefficient vs. number of blades.....	41
Fig. 2.23 Extracted power vs. number of blades.....	42
Fig. 2.24 Power coefficient vs. blade's root length	44
Fig. 2.25 Extracted power vs. blade's root length	44
Fig. 2.26 NACA 0015 extracted power vs. inflow current speeds ($\theta_p = 0$)	46

Fig. 2.27 NACA 0015 extracted power vs. low inflow current speeds ($\theta_p = 0$)	46
Fig. 3.1 A schematic of a foil.....	50
Fig. 3.2 X_1 vs. X_2 response surface plot (CCD) and the optimal response direction.....	52
Fig. 3.3 X_1 vs. X_2 contour plot and the optimal response direction.....	53
Fig. 3.4 Half normal plot of Residuals.....	55
Fig. 3.5 Pareto chart.....	55
Fig. 3.6 Normal probability vs. Residuals plot	58
Fig. 3.7 Residuals vs. Predicted plot.....	58
Fig. 3.8 Residuals vs. Run plot.....	59
Fig. 3.9 Predicted vs. Actual plot.....	59
Fig. 3.10 Box-cox plot	60
Fig. 3.11 Residuals vs. factor plot.....	60
Fig. 3.12 Normal probability vs. Residuals plot.....	61
Fig. 3.13 Residuals vs. Predicted plot.....	61
Fig. 3.14 Thickness (A) vs. Camber Place (B) contour plot.....	64
Fig. 3.15 Thickness (A) vs. Camber Amount (C) contour plot	65
Fig. 3.16 Thickness (A) vs. Pitch Angle (D) contour plot.....	65
Fig. 3.17 A, B and C cube plot	67
Fig. 3.18 A and B interaction plot.....	67
Fig. 3.19 B vs. C contour plot.....	69
Fig. 3.20 A vs. B response surface plot	70
Fig. 3.21 C vs. D response surface plot	70
Fig. 3.22 Model prediction vs. actual power	71
Fig. 3.23 Optimized blade's foil shape vs. conventional NACA 0006.....	73
Fig. 3.24 Quadratic model prediction vs. actual power.....	74
Fig. 3.25 Factor B vs. C contour plot for three bladed turbine.....	78
Fig. 3.26 Factor B vs. C contour plot for four bladed turbine	78
Fig. 3.27 Factor B vs. C contour plot for five bladed turbine.....	79
Fig. 3.28 Tidal current turbine blade	79

Fig. 3.29 Optimized ocean current turbine blade.....	80
Fig. 4.1 Rotor 2D basic mesh.....	84
Fig. 4.3 Foil 2D mesh scheme in Flow Simulation (XY symmetry surface).....	86
Fig. 4.4 NACA 6603 mesh scheme at ($\alpha = 15^\circ$) & $Re = 42000$	86
Fig. 4.5 NACA 6603 velocity contour at ($\alpha = 15^\circ$) & $Re = 42000$	86
Fig. 4.6 Eppler 61 mesh scheme at ($\alpha = 15^\circ$) & $Re = 42000$	87
Fig. 4.7 Eppler 61 velocity contour at ($\alpha = 15^\circ$) & $Re = 42000$	87
Fig. 4.8 Eppler 61 velocity contours ($\alpha = 12^\circ$).....	87
Fig. 4.9 Eppler 61 pressure contours ($\alpha = 12^\circ$).....	88
Fig. 4.10 Eppler 61 velocity contours ($\alpha = 15^\circ$).....	88
Fig. 4.11 Eppler 61 pressure contours ($\alpha = 15^\circ$).....	88
Fig. 4.12 Eppler 61 velocity contours ($\alpha = 15^\circ$).....	89
Fig. 4.13 Eppler 61 pressure contours ($\alpha = 15^\circ$).....	89
Fig. 4.14 Eppler 61 velocity contours ($\alpha = 15^\circ$).....	89
Fig. 4.15 Eppler 61 pressure contours ($\alpha = 15^\circ$).....	90
Fig. 4.16 Iteration based 2D lift coefficient history of Eppler 61 at ($\alpha = 0^\circ$).....	91
Fig. 4.17 Iteration based 2D Drag coefficient history of Eppler 61 at ($\alpha = 0^\circ$).....	92
Fig. 4.18 Time based 2D lift coefficient history of Eppler 61 at ($\alpha = 0^\circ$).....	92
Fig. 4.19 Time based 2D Drag coefficient history of Eppler 61 at ($\alpha = 0^\circ$).....	93
Fig. 4.20 Eppler 61 velocity contours at $\alpha = 0^\circ$	95
Fig. 4.21 Eppler 61 pressure contours at $\alpha = 0^\circ$	95
Fig. 4.22 Eppler 61 velocity contours at $\alpha = 4^\circ$	95
Fig. 4.23 Eppler 61 pressure contours at $\alpha = 4^\circ$	96
Fig. 4.24 Eppler 61 velocity contours at $\alpha = 8^\circ$	96
Fig. 4.25 Eppler 61 pressure contours at $\alpha = 8^\circ$	96
Fig. 4.26 Eppler 61 pressure contours at $\alpha = 12^\circ$	97
Fig. 4.27 Eppler 61 pressure contours at $\alpha = 12^\circ$	97
Fig. 4.28 Eppler 61 velocity contours at $\alpha = 15^\circ$	97
Fig. 4.29 Eppler 61 pressure contours at $\alpha = 15^\circ$	98

Fig. 4.30 Eppler 61 2D lift coefficient validation at ($\alpha = 0^\circ$).....	99
Fig. 4.31 Eppler 61 2D drag coefficient validation at ($\alpha = 0^\circ$).....	100
Fig. 4.32 Time based 2D lift coefficient history of NACA 6603 at ($\alpha = 0^\circ$)	100
Fig. 4.33 Time based 2D Drag coefficient history of NACA 6603 at ($\alpha = 0^\circ$).....	101
Fig. 4.34 NACA 6603 velocity contours at $\alpha = 0^\circ$	102
Fig. 4.35 NACA 6603 pressure contours at $\alpha = 0^\circ$	102
Fig. 4.36 NACA 6603 velocity contours at $\alpha = 4^\circ$	102
Fig. 4.37 NACA 6603 pressure contours at $\alpha = 4^\circ$	103
Fig. 4.38 NACA 6603 velocity contours at $\alpha = 8^\circ$	103
Fig. 4.39 NACA 6603 pressure contours at $\alpha = 8^\circ$	103
Fig. 4.40 NACA 6603 velocity contours at $\alpha = 12^\circ$	104
Fig. 4.41 NACA 6603 pressure contours at $\alpha = 12^\circ$	104
Fig. 4.42 NACA 6603 velocity contours at $\alpha = 15^\circ$	104
Fig. 4.43 NACA 6603 pressure contours at $\alpha = 15^\circ$	105
Fig. 4.44 Eppler 61 & NACA 6603 lift coefficient comparison.....	106
Fig. 4.45 Eppler 61 & NACA 6603 drag coefficient comparison	106
Fig. 4.46 Eppler 61 & NACA 6603 lift to drag coefficient comparison	107
Fig. 4.47 Rotor 3D initial generated mesh.....	108
Fig. 4.48 Rotor 3D coarse mesh scheme in Flow Simulation (YZ surface).....	111
Fig. 4.49 Rotor 3D Fine mesh scheme in Flow Simulation (YZ surface).....	111
Fig. 4.50 Rotor 3D Finer mesh scheme in Flow Simulation (YZ surface).....	111
Fig. 4.51 Rotor 3D coarse mesh scheme in Flow Simulation (XY surface).....	112
Fig. 4.52 Rotor 3D fine mesh scheme in Flow Simulation (XY surface).....	112
Fig. 4.53 Rotor 3D finer mesh scheme in Flow Simulation (XY surface).....	112
Fig. 4.54 Fine mesh scheme around the blade tip in Flow Simulation	112
Fig. 4.55 Fine mesh scheme around rotor blade	113
Fig. 4.56 Rotor velocity contours (YZ surface).....	113
Fig. 4.57 Rotor velocity contours (XY surface).....	113
Fig. 4.58 Rotor pressure contours (XY surface)	113

Fig. 4.59 Blade upper surface pressure contours	114
Fig. 4.60 Blade Lower surface pressure contours.....	114
Fig. 4.61 Upper blade surface pressure distribution	116
Fig. 4.62 Lower blade surface pressure distribution.....	116
Fig. 4.63 Schematic of fine mesh scheme.....	119
Fig. 4.64 Rotor Blade deflection calculations with coarse mesh scheme	120
Fig. 4.65 Rotor Blade deflection calculations with fine mesh scheme	120
Fig. 4.66 Rotor Blade deflection calculations with finer mesh scheme.....	121
Fig. 4.67 Leading edge blade deflection in different meshing schemes.....	121
Fig. 4.68 Rotor blade stress analysis.....	122
Fig. 4.69 Rotor blade deflection analysis (Aluminum Alloy 6061)	122
Fig. 4.70 Rotor blade stress analysis.....	123
Fig. 4.71 Rotor blade stress analysis.....	123
Fig. 4.72 Rotor blade stress analysis (ABS M30).....	124
Fig. 4.73 Rotor blade stress analysis (ABS M30).....	124
Fig. 4.74 Various blades' leading edge deflection.....	125
Fig. 4.75 FDM made blades.....	126
Fig. B.1 X_1 vs. X_2 response surface plot (FFD)	151
Fig. B.2 X_1 vs. X_2 contour plot	151
Fig. B.3 X_1 vs. X_2 response surface plot (CCD).....	152
Fig. B.4 X_1 vs. X_2 contour plot	152

List of Tables

Table 2.1. Hub and turbine blades specifications	34
Table 2.2 Modeling results.....	37
Table 2.3 Rotor's low flow current behavior	45
Table 3.1 First optimization design factors.....	50
Table 3.2 Second optimization design factors	50
Table 3.3 Design summary for the four factors and two levels FFD	54
Table 3.4 Design composition and responses	54
Table 3.5 Design composition and responses	57
Table 3.6 ANOVA analysis chart	62
Table 3.7 ANOVA analysis chart	63
Table 3.8 Design summary for the 4 factors 3 levels CCD design	66
Table 3.9 ANOVA analysis chart	66
Table 3.10 Design composition and responses	66
Table 3.11 Design summary for the 4 factors 3 levels CCD design	68
Table 3.12 Design composition and responses	68
Table 3.13 Factors and responses constraints	74
Table 3.14 Design composition and responses	74
Table 3.15 Factors and responses constrains	74
Table 3.16 Design composition and responses	75
Table 3.17 First optimization's validation	76
Table 3.18 Second optimization's validation	76
Table 4.1 Problem parameters.....	84
Table 4.2 Problem parameters.....	108
Table 4.3 Mesh information	110
Table 4.4 Mesh result progress rate and torque error.....	110
Table 4.5 Aluminum Alloy 6061 material properties	117

Table 4.6 Duraform PA material properties.....	117
Table 4.7 ABS M30 material properties	117
Table 4.8 Mesh details	118

Nomenclature

Symbols

A	: Area of the rotor
a	: Axial induction factor
a'	: Tangential induction factor
B	: Number of blades
c	: Foil chord length (m)
C	: Coefficient
D	: Drag (N/m)
F	: Prandtl's correction Factor
L	: Lift (N/m)
M	: Momentum
\dot{m}	: Mass flow rate
p	: Pressure
r	: Radial distance (m)
R	: Radius (m)
Re	: Reynolds number
T	: Thrust
V	: Velocity (m/s)
u	: Speed at rotor plane

Greek Later

α	: Angle of attack (degree)
ρ	: Density (Kg/m ³)

ν	: Kinematic viscosity (N.m-2.s)
Γ	: Vortex filament of strength
θ	: Pitch angle (degree)
ϕ	: Flow angle (Degree)
ω	: Angular velocity of the rotor
λ	: Tip Speed Ratio
β	: Twist of the blade
σ	: Solidity

Subscript

∞	: Infinity
0	: Far upstream (Free stream)
l	: In the wake
cv	: Control Volume
e	: Effective
g	: Geometrical
i	: Induced
a	: Axial
d	: Drag
l	: Lift
n	: Normal
m	: Momentum
p	: Power
rel	: relative
rot	: Rotational
t	: Tangential
T	: Thrust

List of Appendices

Appendix A. Clarifications on Blade Element Momentum Theory Formulation	145
Appendix B. Introduction to Design of Experiments	148
Appendix C. CFD Governing Equations	153

To my loving wife Nafiseh and family

Chapter 1

Introduction

Renewable energies are becoming more acceptable and commercially viable in recent years due to the adverse effects of environmental pollution and the increasing cost of fossil fuels. Depending on availability of regional solar, wind and water resources, it is possible to fully or partially lessen the consumption of the fossil fuels through employing hybrid or standalone solar, wind or water powered generation units. However, considering the available wind and water energy harvesting techniques, generated clean energy cannot fully address the energy demand. Thus, fossil fuels will still remain the main source of energy.

The idea of harvesting renewable energy from wind in the form of mechanical power is not new. Windmills have historical application in pumping water for agricultural means, milling grains, cutting wood and supplying water. However, converting mechanical power to electricity is a recent technology compared to the history of windmill usage. This conversion has totally changed the role and importance of turbines in today's modern industry to the point that any large scale electric power plant counts on using a type of turbine power generation technology. In general, a turbine is a device that uses fluid flow to produce rotational mechanical power through one or a series of blades, scoops or curved vanes [1], [2]. There are various types of turbines which can be particularly designed to operate with steam, liquid water and gas. In steam turbines, the

thermal energy converts water to super critical steam. The steam thermal energy is then absorbed by the turbine and converted to rotational mechanical energy [3]. In gas turbines, compressed air is pumped into a combustion chamber and then the chamber exhaust containing fuel burnt residuals drives the turbine [4]. Both gas and steam turbines share the same base technology of extracting the thermal/kinetic energy from a gas or steam like flow. On the other hand, harvesting renewable energy from water, which is called hydropower, is somehow different.

The main reason for calling hydropower a sort of renewable energy is that in this method the water, which is available from rain, rivers and ocean, is not consumed and is available with lower internal energy densities after the power extraction process. Hydropower is one of the most common methods of large scale electricity generation. The “conventional” hydroelectric methods take advantage of the water potential energy by blocking the water flow path and creating a water-head or pressure difference by constructing dams or barrages [5]. The other basic type of power plant is the “run-of-river” hydro plant. Here, the water is redirected to the power house and turbine which are normally at lower altitude compared to the river base. The run-of-river plant water storage is considerably smaller and in some cases uses no pondage at all. Thus, the environmental impact is reduced significantly compared to dam construction. It should be noted that the diverse effect of seasonal river flow changes can be regulated through the damping characteristics of the pondage [6]. In both cases, a “Pumped-storage” method may be placed in the power plant in order to do load balancing. This is simply a reservoir that stores the pumped water from lower to higher (reservoir) elevations. During low

electricity demand, extra power is used to pump water to the reservoir and at high electricity demand, the reservoir can be discharged and generate extra electricity [7]. Another kind of hydropower plant which is not common today is the watermill. The watermill takes advantage of free flowing or falling water to turn a large wooden or metal wheel with a number of buckets or blades placed on its outside circumference. The wheel can be mounted vertically or horizontally and driven by either a mill pond or river stream [8].

Hydro power generation utilizing all of the above mentioned technologies requires blocking or redirecting the water path. This is considered to be non-environmentally friendly. To reduce this drawback and also to decrease the power generation unit size, which in turn increases the mobility and maintenance ease of the system, hydrokinetic renewable power generation is introduced. Hydrokinetic energy harvesting is among the most recognized sources of clean energies and it is also a promising technology which can generate electricity from water kinetic energy through using a turbine or a non-turbine system. In general, extractable hydrokinetic sources of energy in the water consist of available kinetic energy in rivers, streams, ocean and tidal currents, wave motions and natural or man-made channels [9], [10]. In Canada, within the Atlantic, Pacific and Arctic coastal currents, the ocean renewable energy is expected to have a noticeable share of country's future energy sources. Accordingly, among various methodologies of harnessing clean ocean energy, major research work has been performed on tidal current and wave energy related technologies [11], [12], [13]. The ocean wave energy industry is based on harvesting the ocean's water surface up and down motion energy which is

available around the clock. Compared to wind, solar, biomass and small hydro, extracting energy from waves is steadier and more predictable. In addition, based on the higher density of sea water, the available wave kinetic energy is much higher than wind energy [14], [15].

Ocean tidal energy is highly predictive compared to wind, solar and even wave energy and based on the greater water density, its available energy harvesting potential is much greater than wind [16]. One of the most positive points about the tidal current which makes it quite desirable as a reliable source of renewable energy is its predictability. The reason for this is the source of tidal streams. Tides are driven by the interaction among sun, earth and moon gravitational forces. As a result, the weather condition does not affect the tidal currents while other sources of energy will be affected by rain, cloud, fog or wind. It is worth noting that generally, the high tides are caused by moon gravitational forces that pull water toward the moon in the areas nearer to it. This causes a bulge in the ocean surface in those areas. In addition, there will be another high tides in the ocean surface just in the opposite site as a result of moon pulling the earth away from the ocean water. The areas positioned between these two high tides experience lower ocean water surface heights (low tides) [17]. It is possible to harness the reliable tidal energy through the water head difference from high to low tides. The tidal energy is commercially viable mostly in the sites where tidal maximum current speeds are higher than 2-2.5 m/s. Suitable tidal current sites normally take advantage of a favorable underwater topography such as straits between islands that boost the current speeds [18]. Conventionally, energy harvesting from tidal currents is possible through constructing a

tidal barrage and usage of a turbine-generator set. Another possibility in shallow tidal areas is to build a lagoon which provides the turbine with water flow during the high and low tides when the lagoon is filling and emptying [19]. However, in these ways, marine environment is still affected by building tidal barrages or lagoons. Constructing the infrastructures takes large amounts of money and time resources [20]. To address this issue, tidal fences and turbines are employed as alternatives. In tidal fences, there are no gates installed and fences are open barrages and the horizontal or vertical axis turbines are supported within fence piers and structures. On the other hand, the tidal turbines are more similar to wind turbines which can harvest kinetic energy in the water. They can be deployed in sites with deeper and stronger tidal currents comparing to tidal fences. In addition, tidal turbines are submerged in water out of sight. Compared to gated barriers and tidal fences, the turbines' environmental effects are limited but still affect fish [21].

The ocean and tidal currents and wave based hydrokinetic energy methodologies will be booming in the next five years in North America and Europe because of carbon regulations and marine renewable energy advances and goals [22]. As mentioned earlier, tidal current and wave energy related technologies have already been receiving considerable attention in Canada. On the other hand, low speed ocean/marine current related energy harvesting technologies have not been extensively explored or addressed in the literature previously so there is potential for research and development in this sector. One of the main characteristics of low speed ocean currents which make them commercially undesirable as a potential renewable power generation alternative is the low available kinetic energy in these currents. Oceans contain currents at nearly all

depths in which the speed and direction can differ in various water heights. Although, the origins of these currents are rather complex, the effects of sun and earth rotation are the most dominant ones. Temperature difference in atmosphere can result in air convection currents called wind. Wind can affect the ocean surface currents but this driving force will fade eventually at depths of more than 100 m [23], [24], [25]. Correspondingly, temperature difference among various water zones will trigger the salinity and density based ocean currents in deeper depths. In addition, earth rotational speed is also an important element which drives the ocean currents through Coriolis force [25]. Geometrical seabed shapes can be a driving force as well. In this way, water will be accelerated due to conversion of its potential energy in higher seabed elevations into water current kinetic energy in deeper regions. Ocean currents, regardless of their origins, are sources of renewable kinetic energy. As mentioned, the main issue with these currents is their low current speeds. As an illustration, the Labrador Current speed along the eastern edge of Grand Banks, irrespective of seasonal variations and wind effects, is between 0.46 m/s and 0.18 m/s at the depth of 110 m and 380 m. These current speeds are measured along the isobaths with the depth of 400 m [26]. Reynaud, *et al.* demonstrated the current speeds of 0.3 m/s to 0.5 m/s along the Labrador Current shelf edge. However, ocean current speeds vary with the depth of measurements. Normally, they decrease with increasing depth, which in turn depends on the site location [27].

Considering the fact that the available kinetic energy in a flow has a cubic relationship with the flow speed, the available energy in the flow with the speed of 0.2 m/s compared to flow speeds of 2 m/s is a thousand times less [28]. This makes the

energy harvesting commercially impossible. However, to power under-water micro sensor systems which are placed in inaccessible locations, the power density appears to be quite suitable based on the application. Therefore, the harvest of even a watt of energy from ocean currents can power a stand-alone micro-sensor package which can have applications in geoscience, earthquake analysis and even military applications [29], [30].

As mentioned earlier, a turbine system is one of the primary options for harvesting ocean current energy. Technological advances, simplicity of design and low cost deployment are among the benefits that highlight this method. Having flexibility to choose among various types of turbine systems is another factor that makes these systems even more desirable. One of the most efficient types of turbine is the horizontal axis turbine. Here, the rotor shaft is parallel to the stream which makes it necessary to point the rotor along with the current. This can be done by either a simple water vane or an active pitching control system [31], [32]. In addition to the rotor shaft, the gearbox and generator are also normally placed in-line with the rotor and in the wake region. Furthermore, the pressure difference between the upper and lower surface of foil shaped blades will provide the required hydrodynamic driving force [33]. On the other hand, in the vertical axis turbine, the main shaft is situated vertically to the stream direction. In this way, the gear box and generator can be placed out of the water current which is beneficial when the depth of the current is low [34], [35]. In the drag based Savonius rotor type, the startup torque is rather high but it delivers lower efficiencies. Therefore, it cannot compete with higher speed lift based Darrieus type rotors. Savonius rotors can be easily described as hollow cylinders cut in two halves and fixed to a shaft with an S-

shape pattern [36], [37], [38]. In contrast, in lift based vertical axis turbines like Darrieus and Giromills rotors, there are a number of curved or straight foil shaped blades attached to a shaft through their ends respectively [39]. Considering the blade positioning, these types of turbines will be self-starting and they will operate without the need to be faced toward the current. Despite their lower generated torques, compared to their Savonius counterparts, higher rotational speeds and centrifugal forces make them more suitable for electricity generation means. Another type of water turbine is the cross flow turbine. In this type, there is a horizontal shaft where a number of foil shaped blades are welded around the shaft to disks making a cage around the shaft. In other words, it is a vertical axis turbine that is deployed horizontally in the water. They are also called transverse horizontal axis water turbines. The main advantages of these turbines are their low structural complexity and the possibility of connecting them together to harness more energy from the water. However, these turbines have less efficiency apex compared to horizontal axis turbines and they are more comparable to Darrieus vertical axis turbines [40], [41].

There are also some non-turbine approaches in which the power harvesting principles are different from their turbine counterparts. These methods try to convert the kinetic energy to a non-rotating mechanical system. For example, Lift or Flutter Vanes extract the water energy through oscillation of hydrofoils by changing their pitch angles [42]. Piezoelectric material can also convert the existing vibrations into electricity. In the water based technology, the vortex shedding created by a solid body in the water vibrates a flexible polymer membrane and the mechanical stress propagation in the material will

generate electric current [43]. Another technology is called the Vortex Induced Vibration (VIV) method. Here, the vortex shedding in the water current is employed to create oscillating motions in the submerged body [44].

From studying available energy harvesting technologies, it can be understood that each of the mentioned technologies and methods in harvesting kinetic energy from ocean water has its own advantages and limitations. In order to be able to harvest energy from ocean currents with the average near sea bed current speeds of 0.2 m/s, the device should have the lowest environmental impact and size, be robust, need very low maintenance and have a long life time. Considering the time constraints and the stage of technology maturity and research costs, a turbine based technology seems to be an appropriate choice.

1.1 Literature Review of Turbine Based Technology

The development of low cut-in speed turbines has only recently received much attention. Therefore, there is a need to polish the existing technology and optimize it for particular water current regimes of interest. The number of designed low cut-in speed water turbines which have the ability to start power generation at low currents of 0.2 m/s is very limited. There was an approach in 2010 with Darrieus, Savonius and a hybrid turbine which are all vertical axis turbines [45]. In this research, the Savonius turbine had the starter role with a cut-in speed of approximately 0.3 m/s and the Darrieus turbine had the power generation duty which also started to generate power at current speeds of

around 0.3 m/s. In Savonius and Darrieus hybrid turbine, the startup ability of the turbines was boosted up to around 0.2 m/s.

Considering the achievements on vertical axis turbines, the size and complexity of hybrid turbine systems, the horizontal axis turbines seem to be a proper alternative. In horizontal axis turbines, there is a potential of increasing the turbine performance through optimizing the blade shape and therefore escalating the power harvesting efficiency for particular water inflow regimes [46]. Consequently, the system size and complexity can be reduced and it is possible to achieve higher power harvesting efficiency compared to vertical axis turbines [2].

1.1.1 Horizontal Axis Turbine Modeling Techniques

In order to avoid conducting expensive and time consuming experiments and also providing a reliable numerical base for performing the optimization stage, a model of the turbine has to be developed. This model should have the ability of calculating the rotors power and torque based on rotor rotational speeds and pitch angles. In order to be able to perform blade optimization, there is also a need to consider the effect of certain factors like blade number and geometry in the model. To address the above mentioned needs, one of the most well-established turbine modeling techniques is the Blade Element Momentum theory (BEM) which is proposed from Glauert in 1935. This model assumes frictionless flow encounters with the rotor with an infinite number of blades. In this way, there will be no vortex shedding in the wake region behind the rotor and the flow leaves the rotor without any circulations [47], [48]. For the sake of simplicity, the effect of the

number of the blades is disregarded in this model. Prandtl's tip loss factor is then introduced to consider the effect of the finite number of blades [49]. An extra correction has to be performed on the BEM model to make it suitable for the optimization stage. This modification considers the influence of the vortex shedding system in the wake. This will enable us to observe the effect of verifying blade numbers more accurately, especially when the value of axial induced velocity from the wakes is high [47].

Another method to model the incompressible fluid flow around a lifting body is lifting line theory. This theory considers the vortex shedding behind the blade/wing which influences the effective angle of attacks. Reflecting the wake region effect on the velocity diagram of the water, the ideal thrust and power coefficients can be derived from the induced velocity diagram [1]. This model assumes the same infinite number of blade as the BEM model. Here, Goldstein's reduction factor is introduced to correct the circulation factor [50]. Another simplification of lifting line theory is the assumption of non-viscous fluid flows. The thrust can be then corrected on account of considering the viscous flow factor. As is seen, both BEM and lifting line theories can be utilized to develop a turbine model for blade optimization purposes after performing some modifications [1].

1.1.2 Rotor Optimization Techniques

Rotor aero/hydro dynamic optimization plays an important role in viability of a turbine based technology compared to other competitors in renewable energy industry [51]. Accordingly, one of the main primary optimization concerns is the blade shape

considerations which have a crucial impact on controlling the behavior and efficiency of a horizontal axis rotor. Considering the non-linear impact of each blade parameter on the turbine performance, blade design and optimization is a demanding task which needs to be performed for each site [52]. Based on the type of desired optimization, various techniques can be applied. Rotor optimization consists of various objectives, variables and constraints such as the two dimensional foil shapes, twist angle, chord length distribution, pitch angle, number and root and tip lengths of blades [53]. One of the methods that assumes the blade as one structure and then tries to modify the blade through simulating the fluid flow field around the blade is the Computational Fluid Dynamics (CFD) method. However, the resulting modifications from this method have to be experimentally verified which is a financial burden [54]. Other methods are normally dependent on the results from blade discretizing method used in BEM and lifting line theory. In this way, the overall performance of the blade can be demonstrated through summation of the power coefficient of smaller sections along the blade span. Consequently, the whole blade performance is optimized when each section has the apex power coefficient.

Accordingly, foil and wing optimization methods were mainly focused on adjoint formulation techniques, which is a gradient based scheme [55], artificial intelligence and genetic algorithm [52], inverse design method and deferential evolution [56], statistical and regression based approaches like response surface methods [57] and stochastic optimization systems [58]. Most of these techniques are based on verifying the gradient

field's variance related to each or a group of design variables. Afterwards, by following the gradient change direction, the apex of the objectives will be reached [55].

1.1.3 Rotor Computational Fluid Dynamics and Finite Element Analysis

Enforced load distribution from water currents is likely to cause unwanted blade tip deflection. The negative effect of tip deflection can be listed as [59]:

- Rotor hydrodynamic efficiency will be decreased which can lead to major rotor torque and power drop.
- Material fatigue will be increased due to blade tip vibration which may result in fatal structural damage.

Consequently, there is a need to consider blade load distribution and the resultant blade tip deflection and vibration behavior as two necessary stages of the turbine design evaluation procedures. In spite of the fact that the BEM model is suitable for blade designing and optimization purposes, it is somehow limited in load distribution analysis based on its 2D nature [60]. To compensate for this issue, the related water turbine simulations are being performed by CFD simulations. In this way, the hydro dynamic behavior of the rotor and also blade loading distributions can be calculated without the need of being further corrected through the CFD codes [61], [62]. Another issue that can be addressed by CFD simulations is the blade vibration behavior analysis. Accordingly, one of the main blade vibrations sources is the blade/inflow wake interactions. This imposes lift and drag pulsations on the blade as a result of stalling and vortex shedding phenomena in the wake region behind the rotor. Therefore, by simulating the wake

behavior through 2D and 3D rotating/non-rotating blade analysis, important information can be learned about the rotor load distribution and pulsation behaviors [59], [63].

The static pressure loading calculated from the CFD stage can be then used in order to calculate the blade bending and twisting deflections and strain/stress distribution. The response of the rotor blade to the loading distribution is called hydro elastic behavior and requires high computational resources in turbine design and development analysis [64]. Accordingly, in [65], a combined plate element code is used to perform a stress analysis which provides detailed information about the blades. It has to be noted that the prediction of the overall deflection in the blades is rather straight forward based on the linear behavior of the blade. However, this behavior becomes non-linear in the places of local deflection such as tip section. In order to solve non-linear equations, it is common to employ commercial soft-ware in which the simulation results depend greatly on the software calibration and that has to be dealt with carefully [66], [67].

1.2 Thesis Objectives

Considering the novelty and challenges of designing a low speed ocean current horizontal axis turbine, the main objective of the thesis is based on designing a compact rotor which would be able to start power extraction from current speeds of as low as 0.2 m/s. Consequently, the efficiency of the turbine becomes an important issue which has to be addressed properly through rotor system modeling, foil and blade optimization. Another item which has to be further investigated is the system vibrations during the rotor performances. This issue has a crucial impact on the system as long as the blades

are thin and long. Regarding the structural strength of the rotor, the pressure distribution over the blade span has to be also calculated and there is a need to choose proper material in order to prevent the blade tip deflection.

For this means, the behavior of the rotor is investigated through a BEM model and the power map will be analyzed during the steady state loading. The model is then verified with the experimental data from the literature. This model provides us with statistical data which is utilized in the design of experiment software to model the power curve surface versus blade design parameters. A gradient based methodology is then employed to verify the apex of the power curve in various rotor application scenarios. In the next stage, the rotor CFD and Finite Element Analysis (FEA) are applied for the purpose of analyzing the vibration and structural strength which insures a safe rotor performance criterion.

1.3 Thesis Organization

This thesis is divided into five chapters. In each chapter, one step of the rotor design and optimization analysis is accomplished. Each chapter is organized in a way that makes it possible to access desired analysis procedures by topic. In chapter 1, the literature review of the various energy harvesting methodologies from water are discussed and the turbine is introduced as one of the major conventional technologies of water current clean energy harvesting. Characteristics, advantages, drawbacks and limitations of each methodology are explained. In the conclusion, the kinetic ocean energy is demonstrated as one of the topics with high research potential for the next couple of years.

Chapter 2 consists of rotor BEM modeling of a horizontal axis turbine. Prandtl's tip loss factor and the effect of the vortex shedding system in the wake region are also addressed in this model. The accuracy of this model is also verified with experimental data extracted from the literature. This model provides a numerical base for the blade regression modeling and gradient based optimization analysis. The basic role of this model is to calculate the power curve of the rotor in various performance criteria.

The regression based modeling of the rotor power response surface is performed through Design of Experiment (DoE) software in Chapter 3. The surfaces are modeled based on non-linear quadratic formulas consisting of the design variables. The response surface is further searched with the Steepest Ascent Methodology (SAM) which enables us to locate the optimum blade design factors values based on predefined constraints. The suggested two dimensional foil shape and blade geometry factors are then utilized for vibration and structural analysis in chapter 4.

In Chapter 4, two and three dimensional (2D and 3D) CFD analysis of the foil and rotor is provided respectively. In this analysis, a velocity and pressure gradient based mesh generation is employed to solve the related equations. Based on the calculated pressure distribution from of 3D-CFD rotor analysis, the tip deflection of the rotor is examined through a FEA analysis. The results from this chapter suggest a choice of the proper material for the rotor construction and enable us to have an estimation of the rotor start up behavior.

Chapter 5 contains concluding remarks and some suggestions for future work.

Chapter 2

Horizontal Axis Ocean Current Turbine Modeling

Water turbines are normally employed to transfer running water kinetic energy to the turbine blades. Hydrodynamic forces are then applied on blades which make the rotor start rotating around its shaft. This rotational movement can be further converted to electricity via a gear box and generator. Based on the application, various types of turbines can fulfill the energy harvesting task. However, horizontal axis turbines provide the highest efficiency regarding their lift based driving forces resulting from foil shaped blades. A detailed description of hydrodynamic power and efficiency sources of this kind of turbines is provided in this section of the thesis.

This chapter focuses on providing an accurate steady state mathematical model of horizontal axis turbines' power harvesting behaviors which has the ability to include the effect of the blade shape parameters such as foil shape profile, chord, tip and root lengths and thickness variations in the rotor performance. To address these needs, the ideal rotor's hydrodynamic governing equations are explained through the well-established Blade Element Momentum theory (BEM) [47], [48], [49]. The accuracy and performance criterion of the ideal model is escalated with Prandtl's tip-loss and Glauert correction factors respectively to accommodate the low cut-in speed characteristics of the rotor. Finally, the model is validated with experimental data available in the literature. It has to be noted that considering the previous work done on BEM modeling techniques, it is not

the scope of this thesis to develop an extension to already available models, but to try developing a model which is an efficient alternative to provide the necessary rotors' operational information for the statistical based optimization stage which is explained in chapter 3.

2.1 Blade Hydrodynamics Theory and Vortex System

In this modeling and to simplify the mathematical formulation, it is assumed that the span-wise velocity of fluid is negligible compared to the flow in the axial and tangential directions. In this way, the hydrodynamic forces on two dimensional (2D) foil shape elements of the blade can be analyzed separately. As a result, the overall driving forces from fluid can be calculated through integration of these 2D blade elements hydrodynamic behaviors. This assumption cannot represent the accurate rotor power generation behavior until the three dimensional (3D) effect of the rotor rotational speed is included in the mathematical formulation of the code. Accordingly, it is necessary to consider the free vortexes phenomenon in the wake behind the blade when the angle of attack α is low. These swirls and spiral motions in the fluid induce a lift force which in turn can be broken into the axial and tangential factors. These factors are called induced lift and drag forces and, based on their time dependent characteristics in the turbulent wake, are difficult to predict. Moreover, the estimation process of these factors is easily affected through rotor rotational speeds and flow separation in the blade's trailing edge. This makes it even more challenging to calculate these forces in the computer used code [68]. In order to start the BEM modeling, the two and three dimensional hydrodynamics

formulations of the blade need to be reviewed and stated. Afterwards, the BEM modeling can be initiated with the help of “actuator disk model” modeling technique [69].

2.1.1 Lift and Drag Forces

A schematic of a rotor is presented in Fig. 2.1. As demonstrated in the above paragraphs, it is possible to divide the blade into several elements. By introducing some correction factors, these smaller sections can be considered two dimensional. A two dimensional foil shape of the blade is exhibited in Fig. 2.2. The foil incident undisturbed flow has to be separated into two directions. One is passing over the upper part of the foil which is accelerating based on the curvature of the foil shape.

In general, fluid responds to the surface curvature through creating a pressure gradient. This pressure gradient acts as a potential to drive the flow slower or faster in the vicinity of the surface. In this case, the upper section of the foil will impose a negative pressure gradient which leads to positive flow speed acceleration. On the other hand, the surface curvature induces a positive pressure gradient over the lower foil surface. As a result of the pressure difference between its lower and upper parts, the foil is lifted upward and the force R is perpendicular to the foil chord. Figure 2.2 demonstrates that this force can be decomposed into a lift component L which is perpendicular to the direction of the inflow fluid V_∞ and a Drag D component parallel to the flow velocity. Lift and drag forces can be expressed through the formulas below [70]:

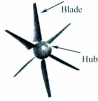


Fig. 2.1 Six bladed horizontal axis rotor

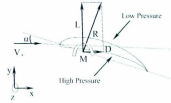


Fig. 2.2 Foil's lift and drag visualization

$$L = 0.5C_l\rho V_\infty^2 c \quad (2.1)$$

$$D = 0.5C_d\rho V_\infty^2 c \quad (2.2)$$

For a particular foil, lift and drag coefficients are dependent on the angles of attack and flow current Reynolds numbers. Lift and drag coefficients of NACA 0015 are plotted versus angles of attack in various Reynolds numbers in Figs. 2.3 and 2.4 [71], [72]. The Reynolds number formula is stated in (2.3) [70]. It is seen that by increasing the Reynolds number, the foil stalling point is delayed to higher angles of attack. As a result, the drag coefficients jump is retarded and the lift coefficients reach higher values. This will increase the lift to drag ratio which is an important factor in rotor design.

$$Re = \frac{cV_\infty}{\nu} \quad (2.3)$$

2.1.2 Vortex System

In order to include the three dimensional effect, it is necessary to consider the vortex system behind the blade trailing edge.

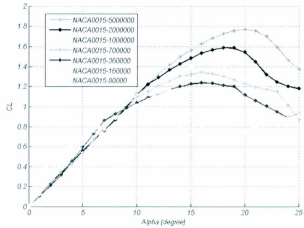


Fig. 2.3 NACA 0015 lift coefficient vs. angles of attack, data is extracted from [71]

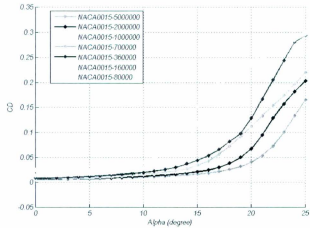


Fig. 2.4 NACA 0015 drag coefficient vs. angles of attack, data is extracted from [72]

To accomplish this, a series of vortices are assumed to be formed near the trailing edge which are further extended into the wake. The vortices on the blade and in the trailing edge are called bound and free vortices respectively [47]. These swirls impose a velocity on any submerged body around them. As a result, a downward velocity is induced in front of the blade which will redirect the undisturbed flow current speed vector from V_∞ to V_e and therefore influences the effective angle of attack, see Fig. 2.5. As a result, there will be an induced angle of attack α_i which has to be deducted from the geometric angle α_g and form the effective angle of attack α_e . Considering the effective angle of attack instead of its geometric counterpart, the 3D lift and drag components will be lower and higher than the 2D lift and drag forces [73].

In order to be able to formulate the 3D effect of rotation in the rotor power calculations, Fig. 2.6 demonstrates the relative velocity which is the effective inflow velocity acting on the blade with the angle of attack of Φ . Accordingly, the induced axial and tangential velocities are opposing the V_a and in the direction of V_{rot} respectively.

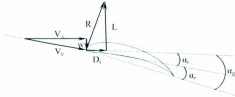


Fig. 2.5 Geometric, effective and induced angle of attacks



Fig. 2.6 Axial and rotational velocities

These velocities are specified through axial and tangential induction factors of a and \hat{a} . The induced axial and tangential velocity components can be stated as aV_0 and $2\hat{a}\omega r$ which are opposing V_a and V_{rot} . Because the flow in the rotor upstream is non-rotating, the induced tangential velocity component will become $\hat{a}\omega r$ and in the direction of the rotor rotation, see figure 2.6. Consequently, the angle of attack can be formulated as below [47],

$$V_a = (1 - a)V_0 \quad (2.4)$$

$$V_{rot} = (1 + \hat{a})\omega r \quad (2.5)$$

$$\phi = \tan^{-1} \frac{(1 - a)V_0}{(1 + \hat{a})\omega r} \quad (2.6)$$

2.1.3 Momentum theory

The momentum theory analysis is applied by considering the ideal actuator disc theory with regard to the frictionless flow and consequently with no swirl or vortices existent in the wake. This theory can be demonstrated through assuming a control volume

around the rotor disc and then applying the momentum equation in axial direction, see equation (2.7) [47]. Where the dA is the area that vector pointing out of each control volume surface with the magnitude equal to the area, F_{pres} is the equivalent of forces applied on the control volume, $d(vol)$ is the volume of each control volume cell. The control volume is exhibited in Fig. 2.7.

$$\frac{\partial}{\partial t} \iiint_{CV} \rho u(x, y, z) d(vol) + \iint_{CS} u(x, y, z) \rho V \cdot dA = F_{ext} - F_{pres} \quad (2.7)$$

Figure 2.7 demonstrates that the main difference between the two control volumes is that there is a mass flow \dot{m} passing through the lateral boundary.

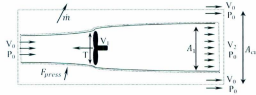


Fig 2.7 Control volumes around the rotor

In contrast, in the second boundary, there is no flow cross passing the boundaries as long as they are aligned with the stream direction. Instead, there will be a pressure distribution along the boundary shown as F_{press} . Considering the steady state flow and solving the axial momentum equations for both control volumes, the rotor extracted power can be formulated as [47]. More information about the origin of the equations (2.8) and (2.9) is provided in the appendix A.

$$P = 2\rho V_0 a(1-a)^2 A \quad (2.8)$$

$$C_p = 4a(1-a)^2 \quad (2.9)$$

Equation 2.9 and Fig. 2.8 show that the maximum power coefficient reached by an ideal horizontal axis turbine is around 0.59 at $a = 1/3$. This limit is called the Betz limit. Accordingly, by increasing the flow blockage in lower rotor rotational speeds, the power extraction will be decreased from its optimum efficiency.

For higher induction factor values, C_T becomes negative which is not feasible and demonstrates the need of further corrections considering the rotation in the wake. Related equations are stated below where the x is the local rotational speed [47],

$$\lambda = \frac{R\omega}{V_0} \quad (2.10)$$

$$P = 4\pi\rho\omega^2 V_0 \int_0^R \dot{a}(1-a)r^3 dr \quad (2.11)$$

$$C_p = \frac{8}{\lambda^2} \int_0^\lambda \dot{a}(1-a)x^3 dx \quad (2.12)$$

2.1.4 Lift and Drag Coefficients

To make the blade optimization stage possible, it is necessary to have access to a comprehensive foil lift and drag data sheet which is mostly unavailable for Reynolds numbers in the range of 20000 to 80000.

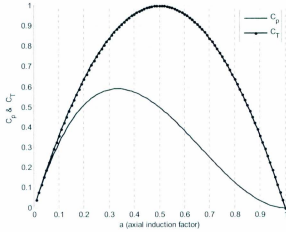


Fig 2.8 Power and thrust coefficients vs. axial induction factor

To address this issue, the XFOIL package is used for numerical 2D foil performance predictions. XFOIL can consider the viscous flows and trailing edge separations (wake modelling) effects in low Reynolds number applications. These abilities made this package ideal for our application [74], [75]. To confidently use XFOIL results for designing purposes, it is important to have a sense of the accuracy of the data. Therefore, NACA 0015 calculated coefficients are validated with experimental values at the Reynolds number of $Re = 80000$ [71], [72], see Figs. 2.9 and 2.10. As is seen in low Reynolds numbers, predicted drag coefficients have a low amount of deviation from experimental values before stalling.

2.1.5 Blade Element Momentum Theory

Regarding the formulation review of one dimensional element theory, it is possible now to apply the momentum theory in the direction of the hydrodynamic lift component which is perpendicular to V_{rel} . There are some assumptions associated with the BEM modeling which make the power calculation possible, but simultaneously, it will impose some limitations and missed calculations. These drawbacks can be further addressed through introducing correction factors which will further modify the model to be suitable for accurate power generation calculations.

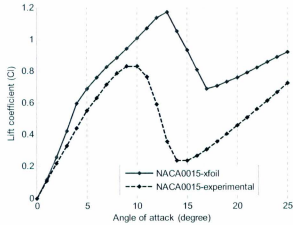


Fig. 2.9 NACA 0015 lift coefficient validation ($Re = 80000$), experimental data is extracted from [71]

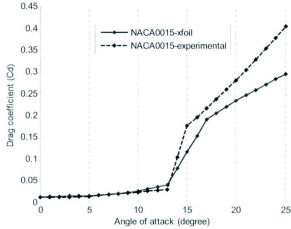


Fig. 2.10 NACA 0015 drag coefficient validation ($Re = 80000$), experimental data is extracted from [72]

The BEM modeling is based on following assumptions,

- The fluid flow is considered to be incompressible and steady state [69]
- There is no radial dependency among blade elements (isolated elements) [76]
- The rotor is assumed to be a disk with an infinite number of blades [76]
- Generated drag has hydrodynamic basis and is not frictional [69]

Applying an integration of momentum equation on the 3D control volume with consideration of local blade geometries, the rotor performance characterization can be calculated through various steps in an iterative manner. To be able to demonstrate these steps and summarize the BEM modeling method, it is necessary to derive the following formulas to calculate the rotor torque and power [47],

$$dp = \omega dM \quad (2.13)$$

To formulate the torque equation, it is necessary to convert lift and drag forces into axial and tangential components, see Fig. 2.11.

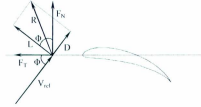


Fig. 2.11 Normal (F_N) and tangential (F_T) components of the total force (R)

Accordingly, the C_n , C_t and dM can be written as,

$$C_n = \frac{F_N}{0.5\rho V_{rel}^2 c} = \frac{L \cos \phi + D \sin \phi}{0.5\rho V_{rel}^2 c} \quad (2.14)$$

$$C_t = \frac{F_T}{0.5\rho V_{rel}^2 c} = \frac{L \sin \phi - D \cos \phi}{0.5\rho V_{rel}^2 c} \quad (2.15)$$

$$dM = 0.5\rho B \frac{V_0(1-a)\omega r(1+a)}{\sin \phi \cos \phi} c C_t \quad (2.16)$$

Now it is possible to apply the integration of tangential forces over the blade span elements in order to calculate the shaft torque. Accordingly, a linear force variation is assumed between two radial elements which varies from $F_{T,i}$ to $F_{T,i+1}$ at the radius of r_i and r_{i+1} , see (2.17) and (2.18). Through defining A_i and B_i , it is possible to describe the torque for each element as (2.19), (2.20) and (2.21) [47],

$$A_i = \frac{F_{T,i+1} - F_{T,i}}{r_{i+1} - r_i} \quad (2.17)$$

$$B_i = \frac{F_{T,i}r_{i+1} - F_{T,i+1}r_i}{r_{i+1} - r_i} \quad (2.18)$$

$$dM = rF_T dr = (A_i r^2 + B_i r) dr \quad (2.19)$$

$$M_{i,i+1} = \left[\frac{1}{3} A_i r^3 + \frac{1}{2} B_i r^2 \right]_{r_i}^{r_{i+1}} = \frac{1}{3} A_i (r_{i+1}^3 - r_i^3) + \frac{1}{2} B_i (r_{i+1}^2 - r_i^2) \quad (2.20)$$

$$M_{tot} = B \sum_1^{N-1} M_{i,i+1} \quad (2.21)$$

After calculating the total rotor shaft torque M_{tot} , it is time to correct the unrealistic effects of infinite number of blade assumption by introducing the Prandtl's tip-loss factor. Considering the vortex system sensitivity to the rotor number of blades, torque equation can be corrected as [47],

$$F = \frac{2}{\pi} \cos^{-1} e^{-f} \quad (2.22)$$

$$f = \frac{B}{2} \frac{R - r}{r \sin \phi} \quad (2.23)$$

$$dM = 4\pi r^3 \rho V_0 \omega (1 - a) \hat{a} F dr \quad (2.24)$$

Another correction is regarding to unreal C_T values when the axial induction factor is becoming more than 0.4. As long as the target of this coding is providing the power generation behavior of the rotor, the thrust calculation has lower interest value in our modeling. However, the axial factor correction presented in the correction procedure will be used in order to provide a faster BEM modeling convergence. Accordingly [47],

$$a = \begin{cases} \frac{1}{\frac{4F \sin^2 \phi}{\sigma C_n} + 1}, & a \leq (a_c = 0.2) \\ f(K) & a \geq (a_c = 0.2) \end{cases} \quad (2.25)$$

Where,

$$f(K) = \frac{1}{2} \left[2 + K(1 - 2a_c) - \sqrt{(K(1 - 2a_c) + 2)^2 + 4(Ka_c^2 - 1)} \right] \quad (2.26)$$

$$K = \frac{4F \sin^2 \theta}{\sigma C_n} \quad (2.27)$$

Where, the solidity of the turbine σ can be expressed as the portion of the control volume which is covered by the blades [47],

$$\sigma = \frac{c(r)B}{2\pi r} \quad (2.28)$$

During each iteration, the tangential induction factor \hat{a} is also updated through (2.29). Finally, the rotor generated power and consequently power coefficient can be calculated for each rotational speed of the rotor through (2.13) and (2.30) [47].

$$\hat{a} = \frac{1}{\left[\frac{(4 \sin \phi \cos \phi)}{\sigma C_t} - 1 \right]} \quad (2.29)$$

$$C_p = \frac{P}{P_{available}} = \frac{P}{0.5 \rho V_{\infty}^3 A} \quad (2.30)$$

After deriving all the necessary formulas, it is possible now to develop the BEM modeling code regarding the desired outputs. Primarily, the rotor and blade specifications have to be fed into the model. Then there are certain steps that have to be solved

iteratively for each of the radial blade elements. Power characteristics of the rotor result from integration of the hydrodynamic forces acting on these elements along the blade span in each rotational speeds of ω . These steps can be summarized as below [47].

- Initialize $a = f(\lambda_i, \sigma(r), \theta_i)$
- Read $C_l(\alpha_i)$ and $C_d(\alpha_i)$ from the XFOIL generated chart
- Calculate $C_{n,i}$ and $C_{t,i}$ through (2.14) and (2.15)
- Calculate $a_{new,i}$ and $\dot{a}_{new,i}$ through (2.25) and (2.29)
- Check the code convergence through a variations tolerance
- Calculate the torque from (2.21)

2.2 BEM Model Results and Validation

In order to visualize and validate the modeling results, the blade's data is extracted based on NACA 0015 characteristics at $Re=2000000$, see Figs. 2.3 and 2.4 [71], [72]. The blade length, chord and pitch angle distributions are adapted from tidal current rotor design available in [76], [77]. These blade specifications are presented in Table 2.1 and Figs 2.12 and 2.13.

As it is seen in Fig. 2.13, the blade thickness is varying nonlinearly along the blade span which alternates the blade profile from NACA 0025 to NACA 0012 based on decreasing the foil thickness from root to tip. This makes the designing and optimization task complex and time consuming.

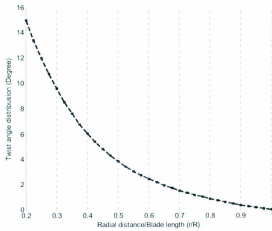


Fig. 2.12 Blade twist angle distribution

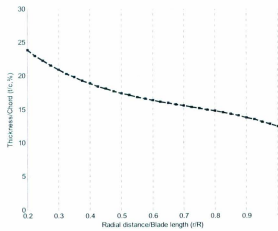


Fig. 2.13 Blade thickness distribution

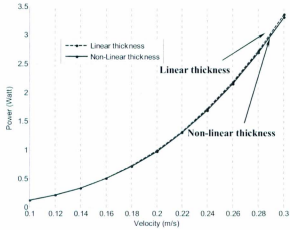


Fig. 2.14 Linear vs. Non-linear blade thickness distribution effect on the rotor generated power

r/R	Radius (mm)	c/R	Pitch distribution (deg)	t/c (%)
0.2	80	0.125	15	23.9
0.25	100	0.1203	12	22.3
0.3	120	0.1156	9.6	21
0.35	140	0.1109	7.65	19.8
0.4	160	0.1063	6.08	18.9
0.45	180	0.1016	4.83	18.1
0.5	200	0.0969	3.85	17.4
0.55	220	0.0922	3.07	16.9
0.6	240	0.0875	2.45	16.4
0.65	260	0.0828	1.95	16
0.7	280	0.0781	1.53	15.6
0.75	300	0.0734	1.19	15.2
0.8	320	0.0688	0.88	14.8
0.85	340	0.0641	0.61	14.3
0.9	360	0.0594	0.38	13.8
0.95	380	0.0547	0.18	13.2
1.00	400	0.05	0.03	12.4

To resolve this issue, a constant foil maximum thickness is chosen for the whole blade length. As is stated in Fig. 2.14, blade thickness variation patterns exhibit

negligible effect on rotor total generated power. In our design, a rotor of a diameter 0.8 m was chosen as a compromise between rotor power generation enhancement and its size. Accordingly, a schematic of a three bladed horizontal axis turbine is presented in Fig. 2.15.

Before further analyzing the BEM model, the power coefficient results are validated with experimental data with the water speed of $V_{\infty} = 1.54\text{ m/s}$ and $\theta = 25^\circ$ [77], see Fig. 2.16. As it is seen, the calculated C_p values in the λ range of three to seven are in good accordance with the experimental values. The reason for this behavior is that when $\lambda < 3$, the turbine still has the unsteady start up performance characteristics and these behaviors cannot be modeled accurately with the developed steady state BEM model of the rotor.

Now, to be able to analyze the model results, the related BEM modeling is tested through a range of rotor performance domain restricted by setting the pitch angles of annular elements between $-5^\circ \leq \theta \leq 15^\circ$, the maximum tip speed to $\omega = 21\text{ rad/sec}$ and the radial element length increments of $dr = 0.01\text{m}$. Calculated power for a three bladed rotor in various inflow speeds is presented in Table 2.2 and Fig. 2.17.

The maximum power is reached when $\lambda \in (6,7)$ which is in accordance with the Betz limit theory. For the purpose of designing a rotor with the ability of operating in low marine currents, this model is considered as a base for further investigating the effects of designing factors on the rotor performance. In this way, the impacts of the pitch angle, tip and root lengths, blade foil shape and number of blades variations on the rotor power generation capability can be analyzed.

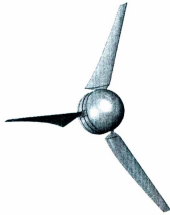


Fig. 2.15 A Schematic of a three bladed rotor

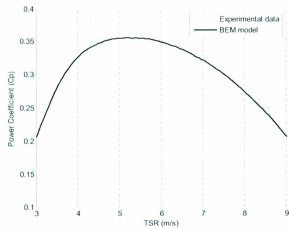


Fig. 2.16 Power coefficient validation

Velocity (m/s)	λ	Theta (deg)	$C_{p,max}$	$P_{max}(kw)$
0.75	6.20	0	0.4893	0.0533
1	6.33	0	0.4900	0.1265
1.25	6.74	0	0.4884	0.2462
1.5	6.17	0	0.4891	0.4260
1.75	6.25	0	0.4893	0.6769

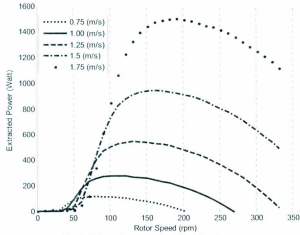


Fig. 2.17 Rotor's power vs. rotor rotational speed

2.2.1 Blade Pitch Angle Effects

As can be seen in Figs. 2.18 and 2.19, when the local pitch angle increases from 0° , the turbine start up capabilities will be boosted up. In order to suggest an operation area for Marine Current Turbines (MCTs), it seems that increasing the pitch angle will be beneficial during the startup process but it will limit the operational λ domain and generated power during the rotor's power extraction mode at the same time.

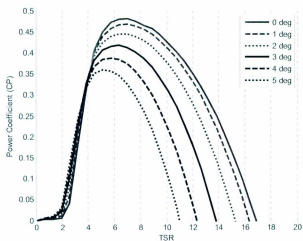


Fig. 2.18 Power coefficient vs. blade's pitch angle ($V_0 = 1 \text{ m/s}$)

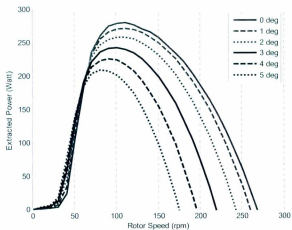


Fig. 2.19 Extracted power vs. blade's pitch angle ($V_0 = 1 \text{ m/s}$)

As an illustration, pitch angle of 5° allows the turbine to reach $C_{p,max} = 0.36$ and has its optimum λ performance criteria in the range of 3 to 7 while these numbers will be upgraded to $C_{p,max} = 0.48$ and λ performance criteria range of 4 to 11 in 0° pitch angle case.

2.2.2 Effects of Blade Length

The NACA 0015 blade length is increased with 0.2 m intervals to see how this element will alter the turbine performance. The results are presented in Fig 2.20 and 2.21.

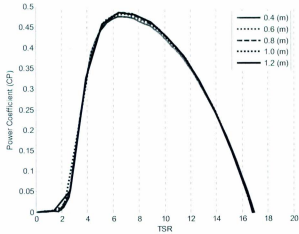


Fig. 2.20 Power coefficient vs. blade length

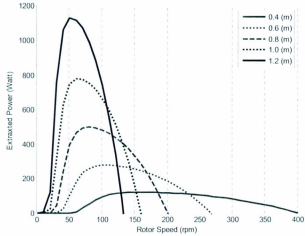


Fig. 2.21 Extracted power vs. blade length

Figure 2.18 shows that by increasing the blade length from 0.4 m to 1.2 m, rotor power coefficient did not show dependency to rotor radius. The maximum improvement in $C_{p,max}$ happened in blade length of 1.2 m which was 2%. On the other hand, power curves shown to be very sensitive to blade length increase while shaft power is almost raised three and nine times when blade length were modified from 0.4 m to 0.8 m and 1.2 m respectively, see Fig. 2.21. Therefore, power curves have also desirably modified to start energy harvesting in quite lower rotor speeds. As it is displayed in Fig. 2.21, power generation is advanced from 50 rpm to 10 rpm by increasing the blade length from 0.4 m to 1.2 m. Moreover, the power reaches to its maximum faster when the blade length is increased. That is quite appealing in low flow

current applications. However, the optimum performance domain of the rotor will be more limited.

2.2.3 Effects of Blade Number

In Figs. 2.22 and 2.23, the BEM model results are presented for various number of blades tuned from 2 to 6. The number of blades is an important option to consider in the rotor designing stage while the imposed restrictions of the energy harvesting environment can be addressed appropriately through modifying the number and geometry of blades. Through adjusting these factors, the rotor would be able to extract optimum kinetic energy from the specific site and as a result, size, weight, efficiency and output power of the rotor could be effectively controlled to guaranty the maximum power generation.

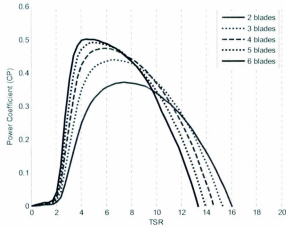


Fig. 2.22 Power coefficient vs. number of blades

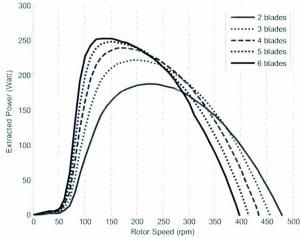


Fig. 2.23 Extracted power vs. number of blades

As can be observed in Fig. 2.22, by increasing the blades number from 2 to 6, maximum power coefficients will be achieved in lower λ values. As illustrated, by increasing the number of blades from 2 to 6, λ is decreased from 7.85 to 4.73 when the inflow speed and rotors radius are $V_{\infty} = 1.25 \text{ m/s}$ and $r_{rotor} = 0.4 \text{ m}$. This means that less rotor rotational speed is required to reach the rotor's performance curve apex while the inflow speed and blade's length are fixed. This fact is beneficial in low cut-in speed rotor designs where the rotor rotational speed is relatively lower than other applications. Another benefit of low current turbine is that when the rotor works with lower rotational speeds, due to less frictional losses, less lubrication is performed, so the maintenance costs and life expectancy of the system are inclined and raised respectively. In general, by having more blades, the rotor gets nearer to ideal rotor assumption and so the induced

vortices are smaller. In this way, turbine should be working with higher efficiencies and lower rotor rotational speed performance domain.

2.2.4 Effects of Blade Shape

In this section, the BEM model was adjusted for a set of runs in which the blade's root chord lengths are modified from 50 mm to 100 mm. This factor restricts the choices on blade numbers while in order to guarantee an acceptable rotor performance enough spacing among blades has to be considered. The modeling results are showed in Figs 2.24 and 2.25. As is apparent, root chord length variations have a similar behavior as changing the rotor blade numbers. But, it is moderated to some extent. As illustrated, by adjusting the root chord length from 50 mm to 100 mm, $C_{P,max}$ and shaft power are raised around 15% and 10% respectively. Moreover, through adding to the length of blade's root chords, rotor optimum performance domain is available in less rotor rotational speeds. As mentioned before, this is a desirable option in designing low marine current turbines. Therefore, the performance characteristics of the turbine are improved through this adjustment.

2.3 Low Flow Current Considerations

In this section, turbine performance in low current regimes is investigated. Turbine's low current operating characteristics are displayed in Figs. 2.26 and 2.27 and Table 2.3.

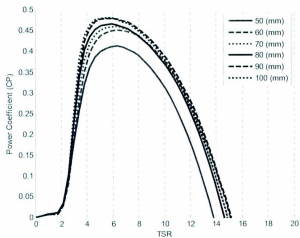


Fig. 2.24 Power coefficient vs. blade's root length

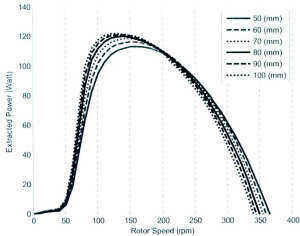


Fig. 2.25 Extracted power vs. blade's root length

From (2.30), it is evident that the output power has a third order relation with inflow speed. This manner is observed in Table 2.3 and Fig. 2.26 as well. Considering the fact that our rotor should harness energy from water velocities between 0.1 m/s to 0.3 m/s , Fig. 2.27 exhibits the turbine performance in this range more clearly. Here, the extracted power at 0.2 m/s is 0.68 Watts which is quite low in order to start the rotor rotating. To address this issue, the rotor start up capability is boosted up through blade optimization which is well explained in the next chapter of this thesis.

2.4 Summary

The harvested power is calculated through formulating the effect of hydrodynamic forces on the blades and then solves them iteratively over the blade elements. The modeling results will form the power response surfaces in chapters 3, which make it possible to model the effect of rotor designing factors on power surface with the assistance of Response Surface Modeling (RSM) techniques.

Current Velocity (m/s)	λ	Theta (deg)	$C_{p,max}$	$P_{max}(w)$
0.1	6.7021	0	0.47622	0.12292
0.2	6.7021	0	0.47622	0.98355
0.3	6.7021	0	0.47622	3.3188
0.4	6.7021	0	0.47622	7.8668
0.5	6.7021	0	0.47622	15.365
0.6	6.7021	0	0.47622	26.551
0.7	6.7021	0	0.47622	42.161
0.8	6.7021	0	0.47622	62.935
0.9	6.7486	0	0.47622	89.609
1.0	6.744	0	0.47623	122.92

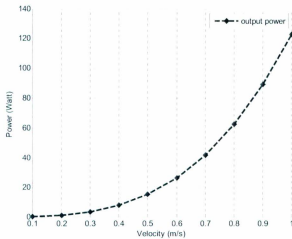


Fig. 2.26 NACA 0015 blades extracted power vs. inflow current speeds ($\theta_p = 0$)

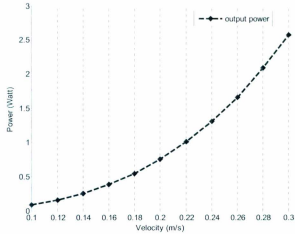


Fig. 2.27 NACA 0015 blades extracted power vs. low inflow current speeds ($\theta_p = 0$)

In the next stage, Steepest Ascent Methodology (SAM) is acquired to optimize the power generation capabilities of the rotor for currents as low as 0.2 m/s through modifying the rotor blades geometry.

Chapter 3

Blade Optimization Using Response Surface Methodology

As long as the effect of the blade geometry characteristics are taken into account in the rotor BEM model, a statistical methodology will be quite resource efficient compared to other foil and blade modeling and optimization techniques [52], [55], [56], [57], [58].

Considering the developed model in Chapter 2, it is possible to statistically model the power response surfaces through Response Surface Methodology (RSM) which is based on a quadratic formula consists of the significant blade geometry design parameters. At this point, the power response contours can be utilized to determine the optimum low Reynolds number blade specifications. At this point, to locate the peak in the power response surface, the Steepest Ascent Methodology (SAM) is employed which takes advantage of power contours gradient direction. In this way, the optimum blade shape can be determined.

3.1 Blade Optimization Descriptions

This section provides a description of a two-step RSM rotor power response surface modeling and optimization. In addition, the related design factors and related restrictions are determined and the applied SAM methodology is explained.

3.1.1 Blade Design Factors and Related Constraints

As can be seen in Fig. 3.1, in order to design a NACA 4-series foil, three factors have to be determined. The first one is the “thickness”, which is the maximum thickness of the two dimensional foil along the chord length. This is expressed by the last two digits of the foil name as the percentage of the chord length. The second factor is the camber amount which is shown by the first digit as the percentage of the chord length. The third one is the camber place which is the second digit of the foil name and expressed in the tens of percentage of the chord length from the leading edge. Apart from the foil shape, as is demonstrated in Figs. 2.18 and 2.19, another significant design factor is the pitch angle which is the angle that each blade is set via the rotor plane. These factors constraints are shown in Table 3.1. Factor A value cannot be less than 3% of the chord length mainly due to the blade machining and performance difficulties. Factors B and C are limited to 2% while lower values cannot have significant effect on the response. Their maximum values are also limited to 9% of the chord length based on the NACA 4-series design configuration.

Another optimization design will be regarding the number of the blades, tip and root lengths. The effects of these factors are demonstrated in Chapter 2. Table 3.2 exhibits the second design factors and their related restrictions. We did not impose the upper limits of the tip and root lengths. They will be determined during the optimization process later.

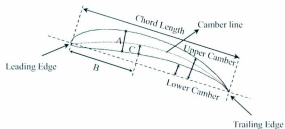


Fig. 3.1 schematic of a foil

Table 3.1 First optimization design factors

Factors and Response	Units	Low	High
Thickness (A)	%Chord	3	100
Camber Place (B)	%Chord	2	9
Camber Amount (C)	%Chord	2	9
Pitch Angle (D)	Degree	-180	180
Power (Response)	Watt	---	---

Table 3.2 Second optimization design factors

Factors and Response	Units	Low	High
Number of Blades (A)	---	3	5
Root Length (B)	mm	10	---
Tip Length (C)	mm	10	---
Power (Response)	Watt	---	---

3.1.2 Statistical Modeling Strategies

The statistical modeling presented in chapter three is a combination of two separate steps. The related design factors and constraints are shown in Tables 3.1 and 3.2. At first, through assuming that there is no nonlinearity among significant factors and response, a two level (2^k) Full Factorial Design (FFD) is considered to investigate if the system

behavior can be modeled with a linear equation [78], [79]. Please find more information regarding the ANOVA and regression analysis in appendix B.

3.1.3 Optimization Methodology

After identifying the significant blade design factors and related power response surface behavior, it is time to explore the modeled region and determine the direction which leads to a domain in the vicinity of the optimum area. For this means, it is best to change the factors in the stepwise manner which in each step, the maximum increase in the response will occur in the direction perpendicular to the contours lines. The movement toward the response surface apex is continued until no significant increase is experienced. At this point, a quadratic model can be utilized to provide more accurate fit to the response. In order to find an optimal response and the related values for each factor, k derivatives with respect to each factor will form k number of coupled equations. By equating these equations to zero, the design factors will be determined. It has to be noted that, to be efficient in this method, a linear regression formula will save us $2k + 1$ runs for each design comparing to a quadratic model where k is the number of factors. Accordingly, Figs. 3.6 and 3.7 demonstrate the direction of the optimal response. The solid lines show the direction that the response increases and leads to a local maximum. On the contrary, the dashed lines exhibit the path that the response is decreasing and aim a local minimum.

3.2 Full Factorial Exploratory Design

A two level (2^k) full factorial design ($k = 4$) is considered first to see if the system behavior can be modeled with a linear model. The data is provided by the BEM model, thus, no random error is expected and no replication is considered in the design. The design center is randomly chosen as NACA 5506 with five degrees of pitch angle. From *FFD* modeling results, we will be able to change the next design center to a point with more desirable response condition.

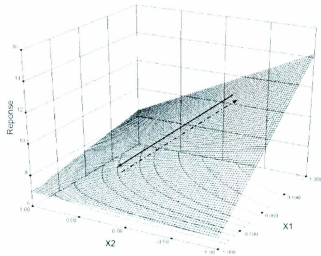
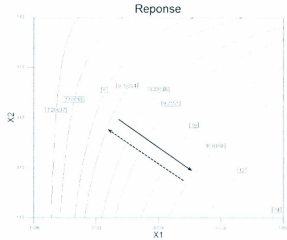


Fig. 3.2 X_1 vs. X_2 response surface plot (CCD) and the optimal response direction



Consequently, it is now necessary to model the response space with RSM which is stated in following sections.

Table 3.3 Design summary for the four factors and two levels FFD

Factors and Response	Units	Low	High
A	%Chord	5	7
B	%Chord	4	6
C	%Chord	4	6
D	Degree	4	6

Table 3.4 Design composition and responses

Run	A	B	C	D	Power
1	5	4	4	4	0.538
2	7	4	4	4	0.388
3	5	6	4	4	0.639
4	7	6	4	4	0.540
5	5	4	6	4	0.487
6	7	4	6	4	0.363
7	5	6	6	4	0.632
8	7	6	6	4	0.530
9	5	4	4	6	0.508
10	7	4	4	6	0.380
11	5	6	4	6	0.587
12	7	6	4	6	0.504
13	5	4	6	6	0.485
14	7	4	6	6	0.369
15	5	6	6	6	0.598
16	7	6	6	6	0.517

3.3 Response Surface Method Design

Because the factorial approach was not able to demonstrate the significant effects in the system, Response Surface Methodology (*RSM*) is utilized to model the existing system non-linearity. Due to having discrete values for *A*, *B* and *C* with related constraints, a faced centered composite design (*CCD*) with one center point is selected for analyzing the response surface.

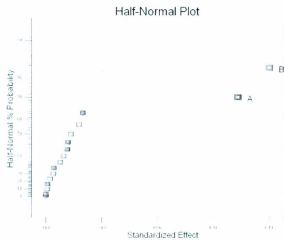


Fig. 3.4 Half normal plot of Residuals

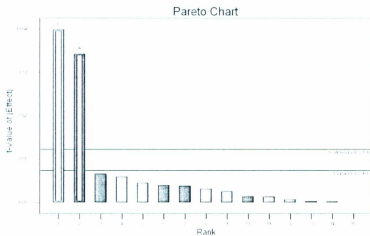


Fig. 3.5 Pareto chart

The reason for choosing the one center point is to see if the model can fit accurately the nonlinear response surface. The nonlinear quadratic model's general form is presented in (3.2). It has to be noted that the third order interactions are omitted from the quadratic model mainly due to generating a less complex model and also their lower effect on response surface behavior. This design has three levels for each factor which mesh well with system constraints. In order to use the steepest ascent method, the smallest possible response space is selected instead of choosing the whole response surface as the modeling domain [81]. In this way, considering the nonlinearity of the system, quadratic equation has a better chance of fitting to the system characteristics. Consequently, it provides a more precise system model which can also be trusted more.

3.3.1 The First Exploratory Design (1st Optimization Step)

We initiated the first design from NACA 5506 with pitch angle of five degrees. The factor domain will be the same as Table 3.5. The number of runs will be $2^k + 2k + 1 = 25$ runs for $k = 4$. In this design, there are sixteen factorial points, eight star points and one center point. The input design composition can be seen in Table 3.5. Due to "Sparsity of effects" rule, only certain effects have significant impact on the system response and therefore have dominant influence on the system model formula. The rest of the effects are utilized to calculate residuals or, in other words, system error. Normality of data and variance distribution are well stated in Figs. 3.10 to 3.17. Figure 3.10 shows that the data is fairly symmetric and unimodal while the residuals stayed close to the fitted line and the s-shape distribution is not observed.

Table 3.5 Design composition and responses

Run	Thickness	Camber Place	Camber Amount	Pitch Angle	Power
1	5	4	4	4	0.538
2	7	4	4	4	0.388
3	5	6	4	4	0.639
4	7	6	4	4	0.540
5	5	4	6	4	0.487
6	7	4	6	4	0.363
7	5	6	6	4	0.632
8	7	6	6	4	0.530
9	5	4	4	6	0.508
10	7	4	4	6	0.380
11	5	6	4	6	0.587
12	7	6	4	6	0.504
13	5	4	6	6	0.485
14	7	4	6	6	0.369
15	5	6	6	6	0.598
16	7	6	6	6	0.517
17	5	5	5	5	0.579
18	7	5	5	5	0.462
19	6	4	5	5	0.446
20	6	6	5	5	0.586
21	6	5	4	5	0.525
22	6	5	6	5	0.516
23	6	5	5	4	0.533
24	6	5	5	6	0.510
25	6	5	5	5	0.526

In Fig. 3.11, residuals are randomly scattered, megaphone shape is avoided and there are no outliers. This means that data variance is relatively the same. Figure 3.12 shows that the residuals are randomly scattered and no trends can be seen, so the mean value is zero. There are no groups of points situated above and below the fitted 45° line in the Fig. 3.13. Thus, the predicted values are not over and under predicted respectively. The Cox-Box plot recommends that a transformation is needed through placing the ($\lambda = 1$) out of the 95% Confidence Intervals (CI). This issue is fixed when the “natural log” transformation is applied, see Fig. 3.14.

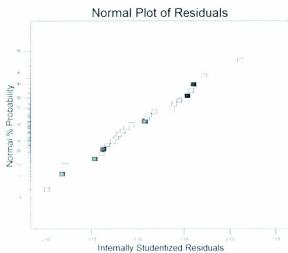


Fig. 3.6 Normal probability vs. residuals plot

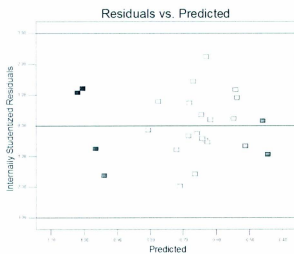


Fig. 3.7 Residuals vs. predicted plot

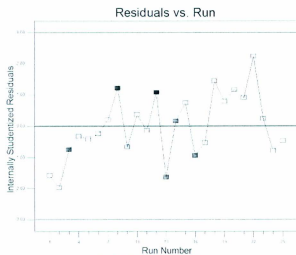


Fig. 3.8 Residuals vs. run plot

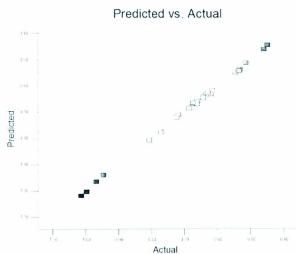
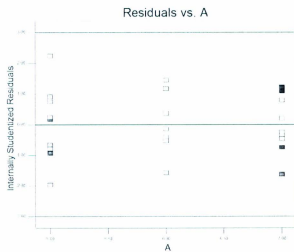
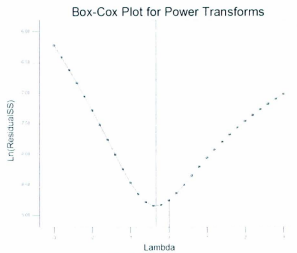


Fig. 3.9 Predicted vs. actual plot



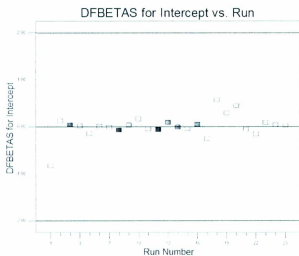


Fig. 3.12 Normal probability vs. residuals plot

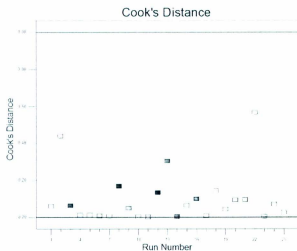


Fig. 3.13 Residuals vs. predicted plot

Figure 3.15 states that the statistical significance of the factors is acceptable. This is shown by random scatter at both ends. As long as all values stay in boundaries, in Figs. 3.16 and 3.17, there is no influential run and no run has to be omitted. After examining the residual fitness, the ANOVA analysis can be performed. The model total p-value in ANOVA analysis is 0.0001. Thus, the model is significant.

Table 3.6 ANOVA analysis chart

Source	Sum of Squares	df	Mean Square	F Value	P-value <i>Prob > F</i>
Model	0.6	14	0.043	1238.5	< 0.0001
A	0.23	1	0.23	6779.37	< 0.0001
B	0.32	1	0.32	9146.84	< 0.0001
C	3.31e-3	1	3.31e-3	95.92	< 0.0001
D	6.73e-3	1	6.73e-3	194.89	< 0.0001
AB	1.41e-3	1	0.018	535.60	< 0.0001
AC	2.85e-5	1	1.38e-4	4	0.0732
AD	1.09e-4	1	6.70e-4	19.37	0.0013
BC	4.60e-4	1	4.05e-3	117.29	< 0.0001
BD	2.60e-4	1	1.73e-3	49.99	< 0.0001
CD	2.12e-4	1	1.70e-3	48.98	< 0.0001
A ²	3.94e-5	1	5.15e-4	14.91	0.0032
B ²	1.59e-4	1	1.81e-3	52.50	< 0.0001
C ²	2.47e-5	1	1.97e-4	5.70	0.0381
D ²	1.65e-5	1	3.45e-5	3.96	0.0745
Residual	6.35e-5	10			
Cor Total	0.072	24			

The p-value or statistical significance testing is examining the probability of generating the calculated results if the considered effects do not exist in reality. When the p-value becomes less than 5%, the ANOVA regression model will be acceptable. As it is seen, all the factors have significant effect on the response expect from AC and D² which their p-values are slightly higher than 0.05. However, these factors were included in the final formula in order to provide a more precise quadratic model. In this model the F-Value is 1238.50 which shows that the model is significant and there is only 0.01%

chance that this value can be generated due to noise. The “R-Squared”, “Adjusted R-Squared”, “Pred R-Squared” and “Adeq Precision” values are exhibited in Table 3.7. The R-Squared value determines how good the model is to predict the response and the value of one shows the perfect match. Similarly, the Adjusted R-Squared represents the goodness of fit. If the value of this variable is smaller than R-Squared value, there are some significant factors missing in the model. The “Pred R-Squared” value has to be in agreement with the adjusted R-squared as well to show the accuracy of the model in prediction. In addition, the “Adequate Precision” is considered as well. This parameter exhibits the signal to noise ratio and assures the designer that adequate signal is used for modeling purposes.

Table 3.7 ANOVA analysis chart

R-Squared	Adj R-Squares	Pred R-Square	Adeq Precision
0.9994	0.9986	0.9957	126.196

In this design, the “Adj R-Squared” of 0.9986 is in a good agreement with “R-Squared” and “Pred R-Squared” of 0.9994 and 0.9957 respectively. The Adeq Precision ($126.163 > 4$) shows the suitable signal availability for the modelling. These tests state that the model represents the design space. Figures 3.18, 3.19 and 3.20 exhibit contours around the design point. By plotting a perpendicular line to the gradient contours in the direction of the maximum response, Figs. will target the *A*, *B*, *C* and *D* values of 5, 6, 4 and 4 respectively. Thus, the previous values are increased or decreased by magnitude of one to meet the new design center point respectively. Therefore, the next design center will be NACA 4605 with 4 degrees of pitch angle.

3.3.2 The Second Exploratory Design (1st Optimization Step)

The second design characteristics are the same as the first design. Modeled response surface domain and designing constraints are shown in Table 3.8. the ANOVA total p-value in this case is 0.0001. The R-Squared, Adj R-Squared, Pred R-Squared and Adeq Precision values are exhibited in Table 3.9. The three different squared parameters are reasonably near to each other which shows that the generated ANOVA model is significant, accurate and no significant factors are omitted from the final formula. The design composition and responses are stated in Table 3.10 and Figs. 3.21 and 3.22. Considering the interactions among *A*, *B* and *C* factors in the cube plot, see Fig. 3.21, their most desirable values would be 4, 5 and 7 respectively.



Fig. 3.14 Thickness (*A*) vs. camber place (*B*) contour plot

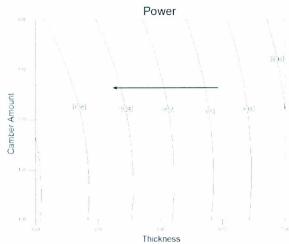


Fig. 3.15 Thickness (A) vs. camber amount (C) contour plot

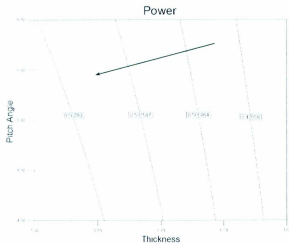


Fig. 3.16 Thickness (A) vs. pitch angle (D) contour plot

Table 3.8 Design summary for the 4 factors 3 levels CCD design

Factors and Response	Units	Low	High
A	%Chord	4	6
B	%Chord	5	7
C	%Chord	3	5
D	Degree	3	5

Table 3.9 ANOVA analysis chart

R-Squared	Adj R-Squares	Pred R-Square	Adeq Precision
0.9926	0.9863	0.9537	49.163

Table 3.10 Design composition and responses

Run	Thickness	Camber Place	Camber Amount	Pitch Angle	Power
1	4	5	3	3	0.661
2	6	5	3	3	0.548
3	4	7	3	3	0.703
4	6	7	3	3	0.655
5	4	5	5	3	0.656
6	6	5	5	3	0.533
7	4	7	5	3	0.767
8	6	7	5	3	0.663
9	4	5	3	5	0.609
10	6	5	3	5	0.515
11	4	7	3	5	0.652
12	6	7	3	5	0.599
13	4	5	5	5	0.627
14	6	5	5	5	0.526
15	4	7	5	5	0.711
16	6	7	5	5	0.640
17	4	6	4	4	0.686
18	6	6	4	4	0.602
19	5	5	4	4	0.605
20	5	7	4	4	0.686
21	5	6	3	4	0.631
22	5	6	5	4	0.646
23	5	6	4	3	0.655
24	5	6	4	5	0.617
25	5	6	4	4	0.639

Consequently, the maximum power is reached with NACA 5704 at pitch angle of 3 degrees. As can be seen, *B* returned to its previous domain in the first explanatory design. This means that this factor is reached its optimum domain and will not be changed further. Figure 3.22 demonstrates the interaction between *B* and *D* when *A* and *C* are in their middle range. As it is seen, the power increases with changing *D* from 5 to 3.

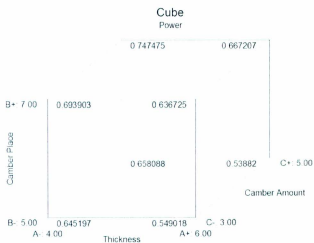


Fig. 3.17 A, B and C cube plot

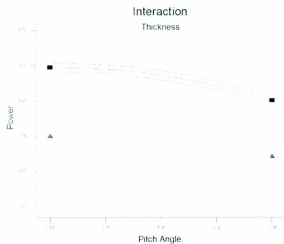


Fig. 3.18 A and B interaction plot

3.3.3 The Third Exploratory Design (1st Optimization Step)

Using the same first design characteristic, the design summary, composition and responses are exhibited in Tables 3.11 and 3.12.

Table 3.11 Design summary for the 4 factors 3 levels CCD design

Factors and response	Units	Low	High
A	%Chord	3	5
B	%Chord	6	8
C	%Chord	4	6
D	Degree	2	4

Table 3.12 Design composition and responses

Run	Thickness	Camber Place	Camber Amount	Pitch Angle	Power
1	3	6	4	2	0.755
2	5	6	4	2	0.659
3	3	8	4	2	0.763
4	5	8	4	2	0.761
5	3	6	6	2	0.796
6	5	6	6	2	0.631
7	3	8	6	2	0.786
8	5	8	6	2	0.731
9	3	6	4	4	0.717
10	5	6	4	4	0.639
11	3	8	4	4	0.746
12	5	8	4	4	0.720
13	3	6	6	4	0.752
14	5	6	6	4	0.632
15	3	8	6	4	0.767
16	5	8	6	4	0.706
17	3	7	5	3	0.766
18	5	7	5	3	0.718
19	4	6	5	3	0.715
20	4	8	5	3	0.757
21	4	7	4	3	0.745
22	4	7	6	3	0.725
23	4	7	5	2	0.781
24	4	7	5	4	0.746
25	4	7	5	3	0.767

The model total p-value is 0.0001 and the R-Squared, Adj R-Squared, Pred R-Squared and Adeq Precision values are 0.9567, 0.9350, 0.9018 and 24.2 respectively. Figure 3.23 exhibits that the camber amount and place contours reached to an apex. In general, the contour curves reach to an extreme where the gradient vector of the response surface is equal to zero and provide the same number of equations and unknowns as significant factors. Consequently, the contour curves are decreasing around this point in any direction. As can be seen in Fig. 3.24, thickness of 3% of the chord length has the highest response values and it is apparent that by decreasing the thickness, more power will be still extracted from the inflow current.

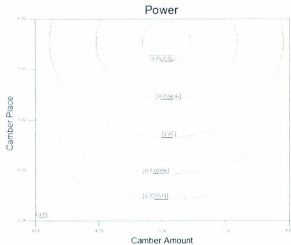


Fig. 3.19 B vs. C contour plot

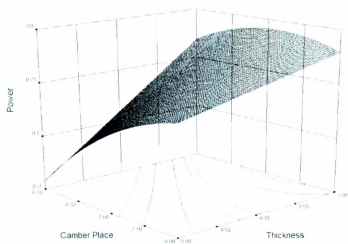


Fig. 3.20 A vs. B response surface plot

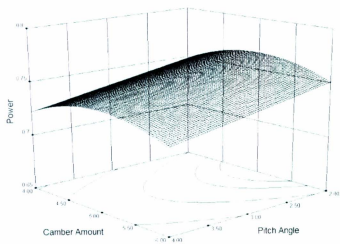


Fig. 3.21 C vs. D response surface plot

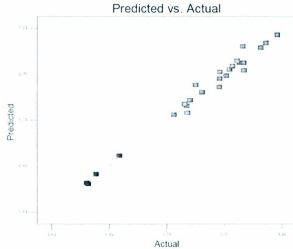


Fig. 3.22 Model prediction vs. actual power

Considering thickness constrains, 3% is chosen as the final A value. Pitch angle of 2 degrees has the highest desirability in our design while it reaches an apex as well, see Fig. 3.25. Figure 3.26 demonstrates high precision of the resultant model while the predicted values close to the $y = x$ line. The resultant quadratic system model is expressed through equation (3.9).

$$\begin{aligned}
 Y = & 0.75 - 0.36A + 0.025B + 0.001C - 0.013D + 0.02AB \\
 & - 0.012AC + 0.002AD - 0.003BC - 0.00007BD \\
 & + 0.002CD - 0.01A^2 - 0.016B^2 - 0.017C^2 + 0.001D^2
 \end{aligned} \quad (3.9)$$

As can be seen in equation (3.9), the Design Expert software is forced to keep the insignificant effects in the quadratic equation. The reason for this is that as long as the

response values resulted from the BEM model, there is no random error in regression analysis. Thus, there will be no need to specify non-significant effects for evaluating the system error. Instead, by including these effects in the final system model and considering their small influence on the response, we would be able to develop a more accurate system model equation. In order to find the optimum response and related factors' value, four derivatives with respect to each factor will form four coupled equations. By equating these equations to zero, which gives us the same number of equations and unknowns as significant factors, NACA 6603 at pitch angle of 2 degrees with response value of 0.783 is calculated as the optimum design choice. Figure 3.27 exhibits the comparison between NACA 3306 and conventional NACA 0006 shapes. The BEM model calculates power value of 0.795 for this foil which shows both the correctness of the optimization and also the high precision of the model.

3.3.4 The First Exploratory Design (2nd Optimization Step)

After optimizing the two dimensional blade's foil shape, optimization is continued by maximizing output power in respect to the blade's root and tip values for different number of blades. The same methodology is applied in this part.

The factor domain and input design composition is shown in Tables 3.13 and 3.14. The model total p-value in this case is 0.0001. The R-Squared, Adj R-Squared, Pred R-Squared and Adeq Precision values are 0.9945, 0.9229, 0.8082 and 18.297 respectively. Thus, the model is significant and it can be trusted for predictions. Figure 3.28 demonstrates that when the number of blade is chosen as 4, by changing the root and tip

length to 70 mm and 10 mm respectively, the output power will be maximized. Thus, tip length constraints have to be kept constant and root length criteria have to be also increased to be able to search for power extremes in the more desirable design domain.

3.3.5 The Second Exploratory Design (2nd Optimization Step)

The second design constraints are set as presented in Table 3.15. Design composition and responses are shown in Table 3.16. The model total p-value in this case is 0.0001.

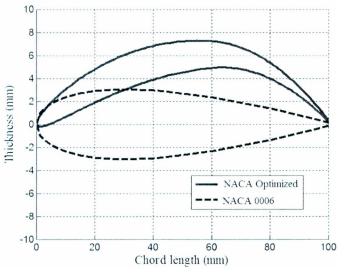


Fig. 3.23 Optimized blade's foil shape vs. conventional NACA 0006

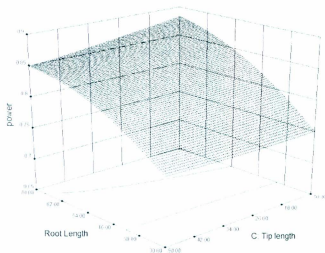


Fig. 3.24 Root vs. tip lengths response surface plot

Table 3.13 Factors and response constraints

Factors and Response	Units	Low	High
Number of Blades (A)	---	3	5
Root Length (B)	mm	30	70
Tip Length (C)	mm	10	50
Power (Response)	Watt	---	---

Table 3.14 Design composition and responses

Run	Number of blades	Root length	Tip length	Power
1	3	30	10	0.653
2	3	70	10	0.833
3	3	30	50	0.702
4	3	70	50	0.806
5	3	50	30	0.782
6	4	30	30	0.757
7	4	70	30	0.867
8	4	50	10	0.853
9	4	50	50	0.817
10	4	50	30	0.823
11	5	30	10	0.829
12	5	70	10	0.909
13	5	30	50	0.795
14	5	70	50	0.881
15	5	50	30	0.864

Table 3.15 Factors and response constraints

Factors and Response	Units	Low	High
Number of Blades (A)	---	3	5
Root Length (B)	mm	70	110
Tip Length (C)	mm	10	50
Power (Response)	Watt	---	---

The R-Squared, Adj R-Squared, Pred R-Squared and Adeq Precision values are 0.9945, 0.9871, 0.9585 and 72.68 respectively. Therefore, the model is significant and is expected to predict precisely. Figure 3.29, 3.30 and 3.31 are demonstrating that a power output apex is reached for various number of blades. This shows that once the most desirable blade is manufactured, different bladed rotors can be assembled with the same blade geometry and expected to work optimally. As can be seen in these figures, the optimum power is constant over a range of tip and root lengths for different numbers of blades. For three bladed turbines, these boundaries are approximately shown through the pointed curve in Fig. 3.29.

Table 3.16 Design composition and responses

Run	Number of blades	Root length	Tip length	Power
1	3	70	10	0.83
2	3	110	10	0.86
3	3	70	50	0.81
4	3	110	50	0.85
5	3	90	30	0.85
6	4	70	30	0.87
7	4	110	30	0.90
8	4	90	10	0.89
9	4	90	50	0.88
10	4	90	30	0.89
11	5	70	10	0.91
12	5	110	10	0.91
13	5	70	50	0.88
14	5	110	50	0.92
15	5	90	30	0.92

3.4 Optimization Validation

Tables 3.17 and 3.18 demonstrate first and second optimization designs validation.

Table 3.17 First optimization's validation

Foil	Pitch angle	Power (RSM)	Power (BEM)	Error (%)
6605	3	0.63	0.636	0.943
6603	3	0.767	0.772	0.648
7503	2	0.79	0.77	2.597
7503	4	0.778	0.75	3.733
6403	3	0.74	0.743	0.404
6403	3	0.653	0.655	0.305
8403	3	0.75	0.755	0.662
8405	3	0.741	0.75	1.2
8603	3	0.777	0.782	0.639
8605	3	0.742	0.72	3.056
6503	2	0.783	0.745	5.101
6503	3	0.77	0.726	6.061
6503	4	0.757	0.745	1.611
6504	2	0.728	0.636	14.47
6504	3	0.714	0.625	14.24
6504	4	0.701	0.625	12.16
6505	2	0.672	0.584	15.07
6505	3	0.658	0.573	14.83
6505	4	0.645	0.564	14.36
7603	2	0.788	0.736	7.065
7603	3	0.801	0.744	7.661
7603	4	0.774	0.713	8.555
8503	2	0.793	0.693	14.43
8503	3	0.779	0.695	12.09
8503	4	0.767	0.664	15.51

Table 3.18 Second optimization's validation

Number of blades	Root length	Tip length	Power (RSM)	Power (BEM)	Error (%)
4	90	10	0.881	0.872	1.03
3	90	30	0.858	0.852	0.7
5	90	30	0.921	0.879	4.8
4	90	30	0.880	0.847	3.9
3	110	50	0.859	0.863	0.46
5	110	50	0.919	0.889	1.76
3	110	10	0.867	0.852	1.76
5	110	10	0.911	0.878	3.76
4	130	10	0.887	0.864	2.66
4	130	50	0.911	0.869	4.83
3	130	30	0.875	0.861	1.62
5	130	30	0.918	0.882	4.08

It is shown that in the first design, due to the high level of nonlinearity, the RSM model is well fitted only near the center of the design and the predictions remain in the 5% Confidence Interval (C. I.). For the modeled spaces far from the center of the design, the accuracy of the model will be decreased to less than 15% of the BEM model calculated results. Having less accurate model in off design center spaces will not affect our methodology while the RSM fitted a quadratic curve that estimates higher power values compared to the BEM model counterparts. In this way, the calculated optimum, which lies in the 5% C. I., will be still higher than other RSM/BEM calculated responses.

On the other hand, the second optimization design predictions remain in the 5% C. I. and the results from the RSM can be trusted.

3.5 Optimization Discussion

Figures 3.32 and 3.33 exhibit both the modified ocean current blade and its conventional tidal current counterpart. The major reason for differences between low ocean current and tidal current blade designs are the change in current speed and consequently the operating blade Reynolds numbers. The Reynolds numbers in tidal currents with average speed of 2 m/s and in ocean currents with average speed of 0.2 m/s are around 200000 and 20000 respectively. By reducing the Reynolds number, thinner foils with high camber amount placed near the trailing edge will generate more lift to drag ratios. This is the reason that a conventional NACA 0006 is modified to NACA 6603 by reducing the operating Reynolds number up to ten times.

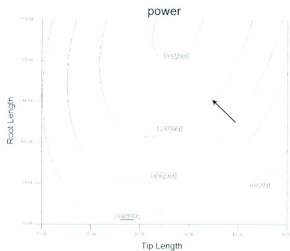


Fig. 3.25 Factor B vs. C contour plot for three bladed turbine

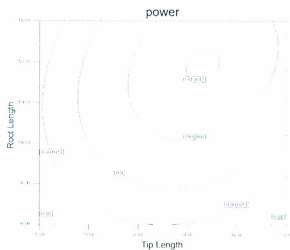


Fig. 3.26 Factor B vs. C contour plot for four bladed turbine

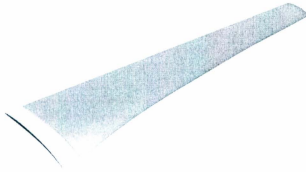


Fig. 3.29 Optimized ocean current turbine blade

The root and tip lengths are also increased to boost the effective energy harvesting surface. It has to be noted that the increase in blades area is limited by their blocking issue which has to be noticed in blade designing stage. As a result of the two-stage optimizations, the turbine output power is increased from 0.13 Watts for conventional NACA 0012 to 0.86 Watts for NACA 6603.

3.6 Summary

In this chapter, an ocean current blade is designed which would be able to harvest energy optimally for average inflow current speed of 0.2 m/s . Due to existing high non linearity dependence among design variables and response, response surface method is used to fit a quadratic equation to the turbine output power response surface. By taking

advantage of steepest ascent method, three and two consecutive faced *CCD* explored the defined system spaces in order to find the maximum response in foil and blade optimization stages. The correctness and accuracy of the optimization are also validated with the developed BEM model. Considering above mentioned optimization stages, it is concluded that by reducing the Reynolds number, thinner foils with high camber amount placed near the trailing edge will generate more lift to drag ratios. Accordingly, NACA 6603 is calculated as the optimum blade shape for the turbine. In addition, it is understood that once the most desirable blade is selected and manufactured, rotors with different number of blades can be assembled with the same blade geometry and expected to work optimally.

Chapter 4

Foil and Blade CFD Analysis

The design evaluation procedure is divided into two stages in this chapter. The first stage focuses is on computing the load distribution generated by the fluid flow. Computational Fluid Dynamics (CFD) calculations are performed with Flow Simulation 2010 package for both validating the optimization results and also calculating the blade load distribution over the blade span. The second stage is more concentrated on blades tip deflection behavior analysis. Simulation 2010 finite element package is used for this means. It is important to note that the reason for recommended simulations is that the designed blade from Chapters 2 and 3 has root, tip and span lengths of 40, 110 and 340 *mm*. Thus the root and tip maximum thicknesses are around 1.2 and 3.3 *mm* which make the blade quite thin compared to its span. Therefore, load distribution created from water currents is likely to cause unwanted blade tip deflection. The negative effect of tip deflection can be listed as: (1) decreased rotor hydrodynamic performance which can lead to major rotor torque and power drop; (2) increased material fatigue due to blade tip vibration which may be resulted in fatal structural damage [82].

4.1 Two-Dimensional Analysis

Flow behavior around Eppler 61 and NACA 6603 foil is investigated through 2D calculations. The 3D calculations need more time and calculation resources which are

beyond the scope of this thesis. Thus, first the correct procedure of the 2D foil simulation with Flow Simulation 2010 is demonstrated through simulating and validating the Eppler 61 lift and drags coefficients [83]. Afterwards, the same procedure is applied for the NACA 6603 and the calculated lift and drag results were compared with experimental Eppler 61 data to measure the low Reynolds performance of the optimized foil.

4.1.1 Two-Dimensional Problem Definition and Parameters

A schematic of the computational domain and the set parameters are exhibited in Fig 4.1 and Table 4.1. As is shown in Table 4.1, the flow is defined as external flow which the cavities and internal flows are disregarded in the simulation. Considering the fact that the problem should be solved in an unsteady mode, the flow is considered to be laminar and turbulent. The unsteady nature of the problem will be stated in section 4.1.3. In addition, the rotor walls are set to adiabatic walls with 70 micrometers roughness. A flow velocity dependency function is also defined to guarantee the Reynolds number of $Re = 42000$ over the foil chord length in the Z direction, see equation (4.1). For this means, a wing with the chord length of 0.125 m is designed and regarded as the testing specimen for the rest of the simulations. The turbulence intensity is also set to 1% [84]. The minimum gap size and the wall thickness are defined as $1e^{-5}\text{ m}$ with default resolution level of 8 with 7 levels of refinements allowance. All the other boundary conditions are set as default which means that mass flow can cross the boundaries without any restrictions.

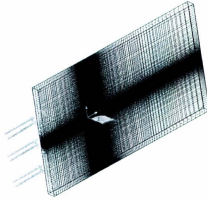


Fig 4.1 Rotor 2D basic mesh

Table 4.1 Problem parameters

Project Configuration	Use current		
Unit system	SI		
Analysis type	External, Exclude cavities without flow conditions & Exclude internal space		
Physical features	Default		
Fluids substances	Water		
Wall Conditions	Adiabatic wall, 70 microns wall roughness		
Initial Conditions	Velocity in Z direction , Turbulent intensity 1% and Turbulence length $9.306e^{-5} m$		
Default geometry resolution	Default result resolution level 8, minimum gap size of $1e^{-5} m$, minimum wall thickness of $1e^{-5} m$ and other options by default		
Fluid space	X (Stream wise)	Min:-0.4m	Max:1 m
	Y (Vertical)	Min:-0.4m	Max:0.4 m
	Z (Cross stream)	Min:-0.0305m	Max:0.0305 m

$$U_{inlet} = \frac{Re \cdot \mu}{L_{Chord} \cdot \rho} = \frac{42000 \cdot 0.0010115}{0.125 \cdot 998.19} = 0.34048 \text{ m/s} \quad (4.1)$$

4.1.2 Two-Dimensional Finite Volume Mesh

The finite volume mesh consists of structured mesh both close to the foil and also in the rest of the domain parts. The basic structured mesh contains 205 and 132 nodes in X

and Y directions respectively of which 82 nodes are along the surface of the foil. The total number of meshes is 60204 after seven levels of refinements allowance. A schematic of the 2D mesh and calculated velocity contours are presented in Figs. 4.3 to 4.7. As it is seen in Figs. 4.4 and 4.5, Flow Simulation refined the basic mesh based on a velocity or/and pressure gradient manner. Dynamic stepwise refinement levels are introduced to the basic mesh in each time step in order to guarantee an essential mesh resolution to provide acceptable precision in the calculations. Formation of laminar separation bubbles and stalling phenomena will induce a high order of velocity and pressure gradient over the foil surfaces. This is the reason that mesh in stalling areas are refined in order to simulate the unsteady dynamics of the problem. It has to be noted that there is one node in the Z direction in either side of the XY symmetry surface.

4.1.3 Time or Iteration Averaging

In order to be able to verify the steady or unsteady nature of the problem, Figs. 4.8 and 4.9 are provided from steady velocity and pressure solutions around the Eppler 61 foil at $\alpha = 12^\circ$. The vortex shedding phenomena is observed in both figures which makes the lift and drag coefficients to be oscillating. In vortex shedding phenomena vortexes are detaching periodically from a solid body sides and are developing further in the back of solid body. The various time instants' pressure and velocity contours are shown for an unsteady solution at $\alpha = 15^\circ$ in Figs. 4.10 to 4.15. The vortex shedding and leading edge boundary layer separation can be observed clearly.

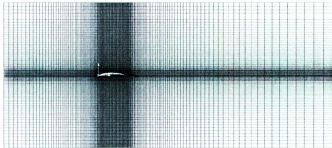


Fig 4.3 Foil 2D mesh scheme in Flow Simulation (XY symmetry surface)

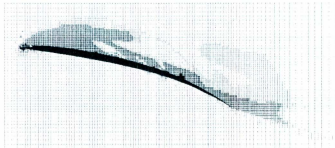


Fig 4.4 NACA 6603 mesh scheme at ($\alpha = 15^\circ$) & $Re = 42000$



Fig 4.5 NACA 6603 velocity contour at ($\alpha = 15^\circ$) & $Re = 42000$

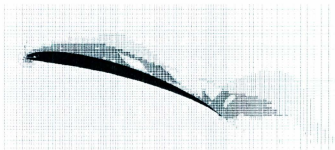


Fig 4.6 Eppler 61 mesh scheme at ($\alpha = 15^\circ$) & $Re = 42000$



Fig 4.7 Eppler 61 velocity contour at ($\alpha = 15^\circ$) & $Re = 42000$



Fig 4.8 Eppler 61 velocity contours ($\alpha = 12^\circ$)



Fig 4.9 Eppler 61 pressure contours ($\alpha = 12^\circ$)



Fig 4.10 Eppler 61 velocity contours ($\alpha = 15^\circ$)
& ($t = 5.5 \text{ sec}$)



Fig 4.11 Eppler 61 pressure contours ($\alpha = 15^\circ$)
& ($t = 5.5 \text{ sec}$)



Fig 4.12 Eppler 61 velocity contours ($\alpha = 15^\circ$)
& ($t = 5.2 \text{ Sec}$)



Fig 4.13 Eppler 61 pressure contours ($\alpha = 15^\circ$)
& ($t = 5.2 \text{ Sec}$)



Fig 4.14 Eppler 61 velocity contours ($\alpha = 15^\circ$)
& ($t = 5.4 \text{ Sec}$)



Fig 4.15 Eppler 61 pressure contours ($\alpha = 15^\circ$)
& ($t = 5.45 \text{ Sec}$)

This means that the problem should be solved in an unsteady mode that enables us to consider the differences in time dependent hydrodynamic characteristics of the foil and provides a time-averaging value of lift and drag coefficients. Accordingly, it is essential that the steady state hydrodynamic behavior of the foil is reached in a time or iteration averaging manner. This will ensure us to consider fully developed hydrodynamic lift and drag coefficients in 2D and 3D rotor power calculations. Accordingly, the iteration averaged lift and drag coefficients formulas is stated below in (4.2) and (4.3) [84].

$$\overline{C_{l,t}} = \frac{\int_{i_0}^i C_l(i) di}{\int_{i_0}^i di} \quad (4.2)$$

$$\overline{C_{d,t}} = \frac{\int_{i_0}^i C_d(i) di}{\int_{i_0}^i di} \quad (4.3)$$

where i_0 is the iteration that the lift and drag simulation is initiated and i is the iteration that the steady state values for iteration averaged lift or drag coefficient are reached. The same formula can be exhibited in time averaging manner.

$$\overline{C_{l,t}} = \frac{\int_{t_0}^t C_l(t) dt}{\int_{t_0}^t dt} \quad (4.4)$$

$$\overline{C_{d,t}} = \frac{\int_{t_0}^t C_d(t) dt}{\int_{t_0}^t dt} \quad (4.5)$$

Similarly, t_0 is the time that the lift and drag simulation is initiated and t is the time that the steady state values for time averaged lift or drag coefficient are reached. The time and iteration based convergences history of lift and drag coefficients of Eppler 61 at ($\alpha = 0^\circ$) are presented in Figs. 4.16 to 4.19. The time/iteration-averaged of these coefficients are also exhibited through the dashed lines.

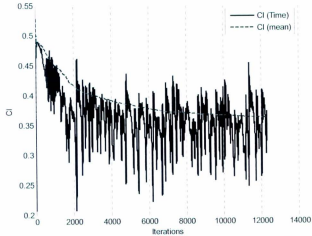


Fig 4.16 Iteration based 2D lift coefficient history of Eppler 61 at ($\alpha = 0^\circ$)

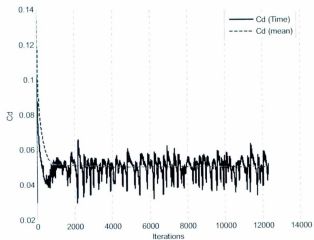


Fig 4.17 Iteration based 2D Drag coefficient history of Eppler 61 at ($\alpha = 0^\circ$)

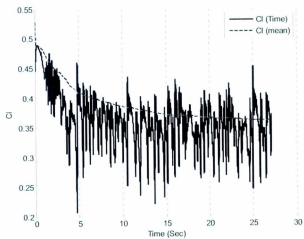


Fig 4.18 Time based 2D lift coefficient history of Eppler 61 at ($\alpha = 0^\circ$)

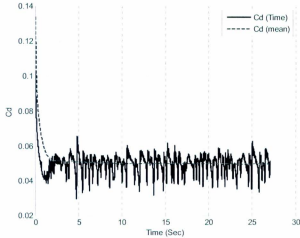


Fig 4.19 Time based 2D Drag coefficient history of Eppler 61 at ($\alpha = 0^\circ$)

The variations of lift and drag coefficient are due to vortex shedding phenomena accruing at the bottom and trailing edge of the foil. Therefore, the lift and drag convergences are monitored based on the error between two consecutive force values which is set to be less than 0.001 in this case. The iteration or time averaged lines are then considered as the stationary value for validation purpose.

4.1.4 Eppler 61 Simulation Results

In order to set a procedure for further calculations of 2D NACA 6603 lift and drag behavior, calculated Eppler 61's lift and drag coefficients are validated with experimental data. The unsteady data is averaged over at least 50 vortex shedding cycles. The time step of calculation is set to 0.0022 Sec which is based on the size of the generated

structured mesh [84]. The experimental data is extracted from the Eppler 61 foil model with span and chord lengths of 30.5 cm and 12.5 cm in a water tunnel with free stream turbulence intensities of less than 1%. The data is available for $Re_{\text{chord}} = 42,000$ with the average uncertainties of 4% for C_l and C_d values [83]. The velocity and pressure contours around Eppler 61 are shown in Figs. 4.20 to 4.29 for various angles of attack. As is seen in Figs 4.4 and 4.6, the mesh around water vortexes got refined automatically by the Flow Simulation as the results are converged. Due to Eppler 61 foil 2D profile shape, adverse pressure gradient causes separation of laminar flow and formation of a separated shear layer near the upper surface trailing edge of the foil at small angle of attacks ($\alpha \leq 10^\circ$). This will degrade the foil performance and diversely affect the lift and drag coefficients. It has to be noted that the laminar separation bubbles form at leading edge of the lower foil surface at $\alpha \cong 0^\circ$. The separated boundary layer reattaches again to foil lower surface however the bubbles are moving toward the trailing edge and join the vortex shedding behind the foil. When the angle of attack increases, flow separation moves toward the leading edge. At $\alpha > 10^\circ$, separation is occurring at the leading edge and it does not reattach to the foil upper surface again which is due to the low operating Reynolds number [85]. Figures 4.20 to 4.29 exhibit the increasing trend of both number and size of bubbles with escalating the angle of attack. It is seen that the bubbles are separating sooner from upper side of the foil, which will consequently increase and decrease the drag and lift coefficients respectively.



Fig 4.20 Eppler 61 velocity contours at ($\alpha = 0^\circ$)



Fig 4.21 Eppler 61 pressure contours at ($\alpha = 0^\circ$)



Fig 4.22 Eppler 61 velocity contours at ($\alpha = 4^\circ$)



Fig 4.23 Eppler 61 pressure contours at ($\alpha = 4^\circ$)



Fig 4.24 Eppler 61 velocity contours at ($\alpha = 8^\circ$)



Fig 4.25 Eppler 61 pressure contours at ($\alpha = 8^\circ$)



Fig 4.26 Eppler 61 velocity contours at ($\alpha = 12^\circ$)



Fig 4.27 Eppler 61 pressure contours at ($\alpha = 12^\circ$)



Fig 4.28 Eppler 61 velocity contours at ($\alpha = 15^\circ$)



Fig 4.29 Eppler 61 pressure contours at ($\alpha = 15^\circ$)

4.1.5 Eppler 61 Simulation Validation

The mentioned trend can also be observed in Figs. 4.30 and 4.31 while by increasing the angle of attack, the lift coefficient will be rather constant or decreasing at $\alpha > 10^\circ$ and drag coefficient will be increasing constantly [83].

4.1.6 NACA 6603 Simulation Results

The same methodology is applied to calculate 2D NACA 6603 foil at Reynolds number of $Re_{chord} = 42,000$. Lift and drag coefficient convergence history of NACA 6603 at $\alpha = 0^\circ$ is visualized in Figs. 4.32 and 4.33. Because the laminar separation bubbles formation is prevented at lower surface of the foil surface, the lift and drag coefficients variations have less domain criterion and also are more regularly spaced comparing to Eppler 61. This allows the foil to experience less intense lift and drag vibrations in lower angles of attack $\alpha < 2^\circ$. This behavior facilitates the energy harvesting task of the blade. According to [86], pressure difference is increasing by

moving from blade root toward the tip in rotating turbines. This will result in the blade tip having more shares in the rotor generated power and torque compared to the blade root. Thus, designing a foil which has the ability to generate higher ratios of lift to drag at $\alpha < 2^\circ$ would be of highest interest when it can effectively boost the turbine efficiency. Considering the water inflow speeds, the Reynolds number in our design is restricted to less than $Re < 40,000$. In these Reynolds number regimes, foils with thin sections and high camber amount at the middle of the foil are suggested [83].

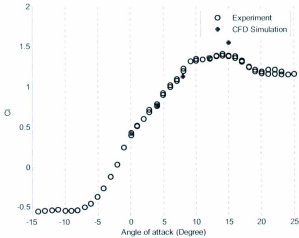


Fig 4.30 Eppler 61 2D lift coefficient validation at ($\alpha = 0^\circ$)

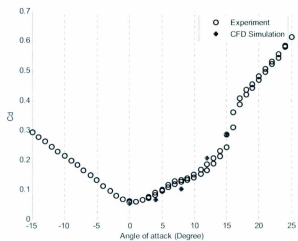


Fig 4.31 Eppler 61 2D drag coefficient validation at ($\alpha = 0^\circ$)

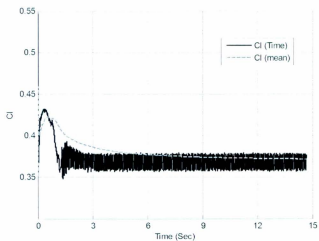


Fig 4.32 Time based 2D lift coefficient history of NACA 66603 at ($\alpha = 0^\circ$)

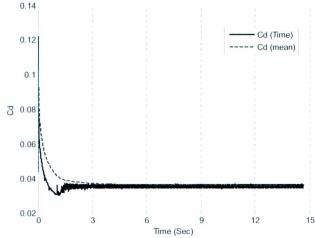


Fig 4.33 Time based 2D Drag coefficient history of NACA 6603 at ($\alpha = 0^\circ$)

With regard to a linear decrease in foil chord length from root to tip, the total thickness of the tip section would be around a millimeter [10]. Thus, structural resistance analysis of the blade's tip against bending and rotational stresses should be included in the design process. Moreover, having probable vibration in this part, absence of careful design can lead to fatal fatigue failures and increase the chance of vibration resonance phenomena. Figures 4.34 to 4.43 exhibit the NACA 6603 simulated hydrodynamic performance in various angles of attack. As it is shown in Figs. 4.44 to 4.46, the NACA 6603 simulated hydrodynamic performance is compared with Eppler 61 experimental data. Accordingly, the lift and drag coefficients are decreased and escalated respectively in NACA 6603 mainly before the laminar separation bubbles formation happens. As a result, lift to drag ratio is increased up to 40%, see Fig. 4.46.



Fig 4.34 NACA 6603 velocity contours at ($\alpha = 0^\circ$)



Fig 4.35 NACA 6603 pressure contours at ($\alpha = 0^\circ$)



Fig 4.36 NACA 6603 velocity contours at ($\alpha = 4^\circ$)



Fig 4.37 NACA 6603 pressure contours at ($\alpha = 4^\circ$)



Fig 4.38 NACA 6603 velocity contours at ($\alpha = 8^\circ$)



Fig 4.39 NACA 6603 pressure contours at ($\alpha = 8^\circ$)



Fig 4.40 NACA 6603 velocity contours at
($\alpha = 12^\circ$)



Fig 4.41 NACA 6603 pressure contours at
($\alpha = 12^\circ$)



Fig 4.42 NACA 6603 velocity contours at
($\alpha = 15^\circ$)



Fig 4.43 NACA 6603 pressure contours at
($\alpha = 15^\circ$)

Considering the fact that the tip part of the blade will generate the main share of the generated torque with the effective angle of attach of $\alpha < 5^\circ$, a proportional increase in rotor energy harvesting capabilities is expected from the case that the blade was constructed from Eppler 61 profile. It is important to note that the Eppler 61 is a conventional low Reynolds number foil and can be a safe choice for rotors performing in $Re = 40000$ region.

4.2 Rotor Three-Dimensional (3D) Startup Considerations

Considering the limited extractable kinetic energy by a rotor with radius of 0.4 m in flow speed regimes of around 0.2 m/s , investigation of the rotor start up capabilities will be crucial [87]. Based on the design of the rotor, a pressure difference will be formed between two surfaces of the rotor blades and consequently a certain amount of startup torque will be applied on the rotor's shaft. As mentioned in Chapter 2, the steady state torque calculations can be performed through the developed BEM model.

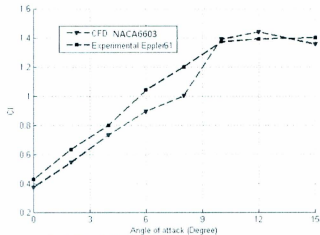


Fig 4.44 Eppler 61 & NACA 6603 lift coefficient comparison

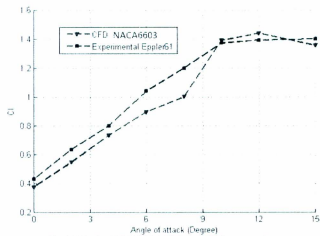


Fig 4.45 Eppler 61 & NACA 6603 drag coefficient comparison

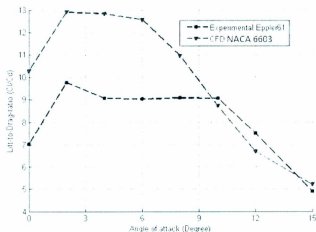


Fig 4.46 Eppler 61 & NACA 6603 lift to drag coefficient comparison

In order to have detailed information of the transient load distribution on the blade surface in the terms of pressure distribution during the startup process, a CFD based approach can be employed. Afterwards, it is possible to perform the blade deflection survey through a FEA analysis. By investigating the tip deflection behavior of the blade, the proper material can be chosen to both facilitate the blade manufacturing process and also guarantee appropriate blade tip deflection behavior.

4.2.1 Three-Dimensional Problem Definition and Parameters

A schematic of the computational domain and the set parameters are exhibited in Fig 4.47 and Table 4.2.

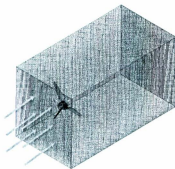


Fig 4.47 Rotor 3D initial generated mesh

Table 4.2 Problem parameters

Project Configuration	Use current		
Unit system	SI		
Analysis type	External; Exclude cavities without flow conditions & Exclude internal space		
Physical features	Default		
Fluids substances	Water		
Wall Conditions	Adiabatic wall, 70 microns wall roughness		
Initial Conditions	Velocity in Z direction 0.2 m/s, Turbulent intensity 1% and Turbulence length 0.03 m		
Default geometry resolution	Default result resolution level 8, minimum gap size of 0.0018 m, minimum wall thickness of 0.0018 m and other options by default		
Fluid space	X (Cross stream)	Min:-0.7m	Max:0.6 m
	Y (Vertical)	Min:-0.7m	Max:0.7 m
	Z (Stream wise)	Min:-0.5m	Max:2 m

As it is demonstrated in Table 4.2, the flow is chosen as external flow simulation in which the cavities are disregarded. It is also assumed that all the rotor joints are ideally sealed, thus, there will be no internal space/flow interaction considerations. Regarding the unsteadiness of the problem and the laminar separation bubbles phenomena, the flow is considered to be part laminar and part turbulent. Moreover, the rotor walls are considered to be adiabatic with 70 micrometers roughness. A flow velocity of 0.2 m/s is set in the Z

direction and the turbulence intensity is set to 1% . The minimum wall thickness is set to 0.0018 m with default resolution level of 8 with 7 levels of refinements allowance. All the other boundary conditions are set as default which means that mass flow can cross the boundaries without any restrictions.

4.2.2 Three-Dimensional Finite Volume Mesh

Similarly, the finite volume mesh consists of structured mesh both close to the foil and in the rest of the domain parts. Three structured basic mesh schemes, “Coarse”, “Fine” and “Finer” are used. The coarse mesh consists of 38, 40 and 68 nodes in X , Y and Z directions respectively. On the other hand, the fine mesh includes 52, 54 and 96 along these three directions while the finer version has 58, 62 and 108 nodes. The total number of cells after seven levels of refinements allowance and their size information are exhibited in Table 4.3. Table 4.4 demonstrates that the calculated torque is in good agreement with the steady state torque calculation from BEM model for the same rotor used for the CFD simulations. The maximum steady state rotor extracted power is 0.87 watt at the rotor rotational speed of 41.3 rpm which equates the torque to 0.201 N.m. Consequently, the ‘fine’ and ‘finer’ meshes show better prediction capabilities of the BEM model results with 2.9% and 1.9% error, thus, both of them can be used for pressure distribution calculations. Considering that the finer simulation is time consuming and the accuracy progress rate is only 1.02%, the fine model results are chosen to be further analyzed in the rest of the thesis.

Table 4.3 Mesh information

Mesh	Solid Cells	Fluid Cells	Min Cell Volume (m^3)	Max Cell Volume (m^3)
Coarse	12359	176457	$1.679e^{-10}$	$4.401e^{-5}$
Fine	56381	395162	$6.439e^{-11}$	$1.688e^{-5}$
Finer	69434	511149	$4.469e^{-11}$	$1.172e^{-5}$

Table 4.4 Mesh result progress rate and torque error

Mesh	Torque ($N.m$)	Result Progress (%)	Error (%)
Coarse	0.189	---	5.9
Fine	0.195	3.17	2.9
Finer	0.197	1.02	1.9

Schematics of the 3D meshes are presented in Figs. 4.48 to 4.53. As is seen in Figs. 4.48 to 4.53, Flow Simulation refined the basic mesh based on a velocity or/and pressure gradient manner. The reason that this behavior is less visible in Figs. 4.48 and 4.53 is that the calculation is stopped based on the set goals convergence. There was no point in continuing calculations after the simulation is converged to let the package generate more visible velocity/pressure gradient mesh refinements.

4.2.3 Three-Dimensional Blade Pressure Distribution

The resultant pressure and velocity contours of the finer mesh scheme are expressed in Figs. 4.56 to 4.58. As it is seen in Fig. 4.57 and 4.58, there is a variable velocity and pressure difference between the lower and upper part of the blades which will act as a desirable driving force.

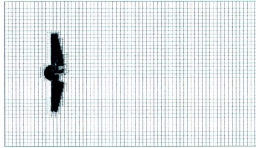


Fig 4.48 Rotor 3D coarse mesh scheme in Flow Simulation (YZ surface)



Fig 4.49 Rotor 3D Fine mesh scheme in Flow Simulation (YZ surface)

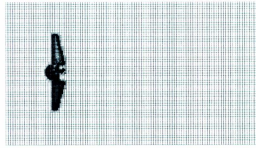


Fig 4.50 Rotor 3D Finer mesh scheme in Flow Simulation (YZ surface)

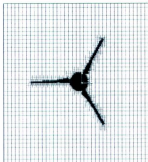


Fig 4.51 Rotor 3D coarse mesh scheme in Flow Simulation (XY surface)

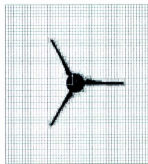


Fig 4.52 Rotor 3D fine mesh scheme in Flow Simulation (XY surface)

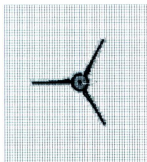


Fig 4.53 Rotor 3D finer mesh scheme in Flow Simulation (XY surface)

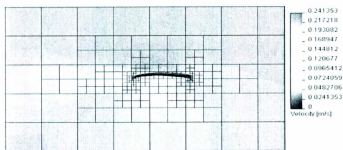


Fig 4.54 Fine mesh scheme around the blade tip in Flow Simulation

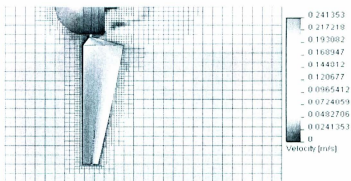


Fig 4.55 Fine mesh scheme around rotor blade



Fig 4.56 Rotor velocity contours (YZ surface)

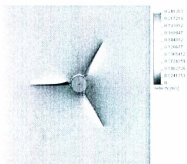


Fig 4.57 Rotor velocity contours (XY surface)

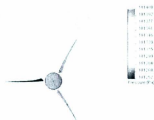


Fig 4.58 Rotor pressure contours (XY surface)



Fig 4.59 Blade upper surface pressure contours



Fig 4.60 Blade lower surface pressure contours

The upper and lower blade surfaces pressure distributions are exhibited in Figs. 4.59 and 4.60. These figures exhibit the pressure difference between upper and lower surfaces of blade schematically. More precise observation can be done through the Figs. 4.61 and 4.62. These figures show that there is a wide variety of average pressure differences which varies between -0.4 Pa to 15.5 Pa among shown sections. Minus values present the undesirable driving force which resist against rotor rotation.

4.3 Finite Element Analysis of Blade Tip Deflection

After calculating the distributed loads on the blades, their tip deflection behavior is analyzed using the Simulation 2010 software. Based on the performed Finite Element Analysis (FEA), appropriate material is chosen for the manufacturing process. Consequently, the excessive blade tip deflection is avoided in the final design.

4.3.1 Manufacturing Processes and Materials

There are three manufacturing technologies available to fabricate the blades in the Memorial University of Newfoundland: Computer Numerical Control (CNC) machine, Selective Laser Sintering (SLS) and Fused Deposition Modeling (FDM) prototype machines. The CNC machine takes advantages of various movable cutting tools which can precisely cut the rotating piece, thus, the part will be finished with the high accuracy of 0.1 mm . In this work, the chosen milling material is Aluminum Alloy 6061. The alloy property is pre-defined in the software library and also expressed in Table 4.5. On the other hand, the SLS technology benefits from utilizing sintered powder materials which are fused together through a high power laser [1]. The SLS process is able to produce parts with tolerance of 0.3 mm . The SLS prototyping material is chosen as Duraform PA which properties are expressed in Table 4.6 [88], [89]. The FDM uses a nozzle to extrude melted plastic in layers to form the part. The tolerance on this method is 0.6 mm . The ABS M30 is selected as the prototyping material which is 20 – 75 percentages stronger than standard Stratasys ABS. Related material properties are exhibited in Table 4.7 [90].

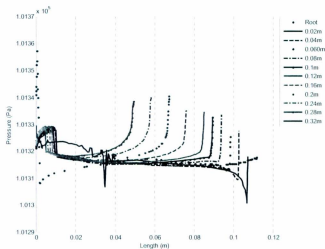


Fig 4.61 Upper blade surface pressure distribution

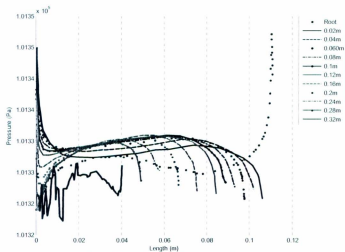


Fig 4.62 Lower blade surface pressure distribution

Table 4.5 Aluminum Alloy 6061 material properties

Property	Value	Units
Elastic Modulus	$6.9e^{10}$	N/m^2
Poisson's Ratio	0.33	N/A
Shear Modulus	$2.6e^{10}$	N/m^2
Density	2700	kg/m^3
Tensile Strength	124084000	N/m^2

Table 4.6 Duraform PA material properties

Property	Value	Units
Elastic Modulus	$1.6e^9$	N/m^2
Poisson's Ratio	0.3	N/A
Shear Modulus	$6.15e^8$	N/m^2
Density	590	kg/m^3
Tensile Strength	$4.4e^7$	N/m^2

Table 4.7 ABS M30 material properties

Property	Value	Units
Elastic Modulus	$2.4e^9$	N/m^2
Poisson's Ratio	0.37	N/A
Shear Modulus	$8.7e^8$	N/m^2
Density	1038	kg/m^3
Tensile Strength	$3.6e^7$	N/m^2

4.3.2 Three Dimensional Finite Element Mesh

In order to be able to obtain converged results from the deflection simulation, three mesh densities are generated and related information is expressed in Table 4.8. As can be seen, the element size and tolerance are halved in each step and made two modified 'fine' and 'finer' mesh schemes from original 'coarse' mesh. A schematic of the fine mesh is presented in Fig. 4.63. To investigate the convergence of the results, the pressure distribution is imported from CFD calculations and the material is set to Duraform PA. Accordingly, Figs 4.64, 4.65 and 4.66 demonstrate the blade's tip deflection calculation results. The results progress rate between 'coarse', 'fine' and 'finer' meshes are 3.62% and 0.97% respectively.

Table 4.8 Mesh details

Mesh Details	Coarse mesh	Fine mesh	Finer mesh
Mesh type	Solid Mesh	Solid Mesh	Solid Mesh
Jacobian points	4 Points	4 Points	4 Points
Element size	10 mm	5 mm	2.5 mm
Tolerance	0.5 mm	0.25 mm	0.125 mm
Total nodes	35543	162180	906489
Total elements	21206	102543	607689
Maximum aspect ratio (AR)	6721.5	829.44	371.44
Percentage of elements with AR < 3	71.5	86.6	96.6
Percentage of elements with AR > 10	3.97	0.716	0.144

Considering the fact that the ‘finer’ simulation is time consuming and the result progress rate is 0.97%, the ‘fine’ mesh scheme model results are chosen to be further analyzed in the rest of the analysis. Figure 4.67 shows the span-wise blade deflection values. Accordingly, the convergence of the results is stated through almost matched fine and finer calculated blade displacements.

4.3.3 Results of Analysis of Blade Tip Deflection

After importing the pressure distribution from CFD calculations, a static FEA analysis is performed on the blades. Three mentioned materials are selected to investigate the related blades tip deflection behavior. In order to prevent unwanted rotor displacement during the calculations, the lower part of the split hub and the rotor shaft are fixed. The FEA calculation outcomes are exhibited in Figs. 4.68 to 4.74. These figures demonstrate that the stress concentrations are in the area of blade root and trailing edge. Thus, in the case of failure, these areas are going to be more vulnerable. In addition, the

maximum tip deflection is seen in Duraform PA blade with Maximum displacement of 3.26 mm .

This value for ABSM30 and Aluminum Alloy 6061 blades is 2.16 mm and 0.075 mm . More precise observation of the blade displacement behavior can be seen in Fig. 4.74. In the end, considering the fact that the CNC made blade costs nearly eight times more than its SLS and FDM counterparts and ABSM30 has more resistance compared to Duraform PA, FDM prototype technology and ABSM30 are selected to manufacture the blades. Figure 4.75 shows FDM made blades.

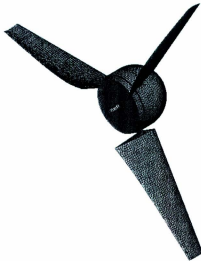


Fig 4.63 Schematic of fine mesh scheme

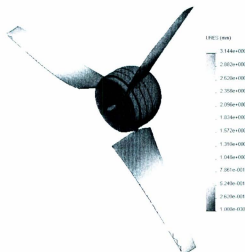


Fig 4.64 Rotor blade deflection calculations with coarse mesh scheme

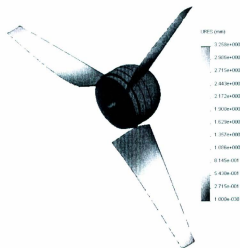


Fig 4.65 Rotor blade deflection calculations with fine mesh scheme

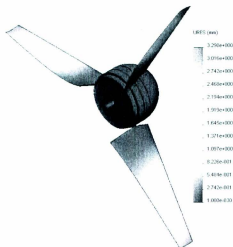


Fig 4.66 Rotor blade deflection calculations with finer mesh scheme

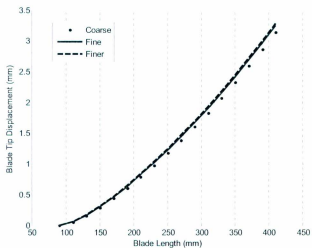


Fig 4.67 Leading edge blade deflection in different meshing schemes

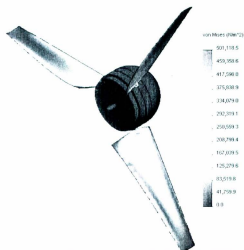


Fig 4.68 Rotor blade stress analysis (Aluminum Alloy 6061)

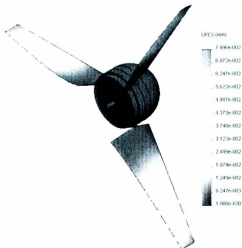


Fig 4.69 Rotor blade deflection analysis (Aluminum Alloy 6061)

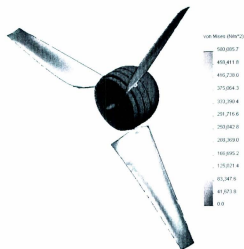


Fig 4.70 Rotor blade stress analysis (Duraform PA)

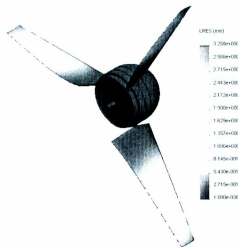


Fig 4.71 Rotor blade deflection analysis (Duraform PA)

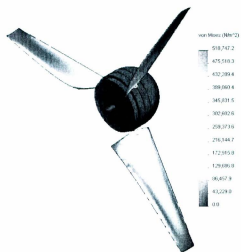


Fig 4.72 Rotor blade stress analysis (ABS M30)

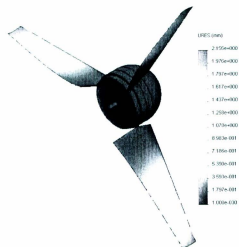


Fig 4.73 Rotor blade deflection analysis (ABS M30)

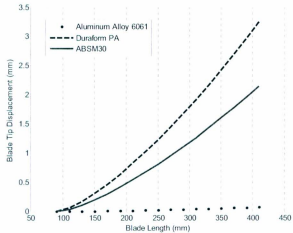


Fig 4.74 Various blade's leading edge deflections

4.4 Summary

In this chapter, a CFD approach is utilized to calculate the generated startup torque and blade's pressure distribution of the designed rotor. Afterwards, the CFD calculated load distribution is imported from CFD to a finite element analysis package in order to model the blade deflection during the rotor startup. Finally, the calculations suggest proper manufacturing methods and materials to avoid excessive deflection in rotor optimized blades.

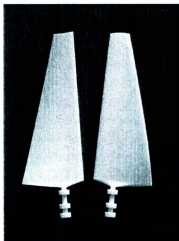


Fig 4.75 FDM made blades

Chapter 5

Conclusions

5.1 Summary

Low cut-in speed rotors enable us to harvest renewable energy from low speed water streams. Considering the well-established wind/water turbine technology, it is practical to design a compact rotor to extract energy from currents with flow speeds of 0.2 m/s . Accordingly, a reliable source of renewable energy can be deployed on the seabed which is cheap, compact and simple in design and also requires low maintenance cost.

This thesis has discussed a novel methodology to model, design and analyze a horizontal axis rotor. In Chapter 2, the conventional *BEM* model theory with two corrections is chosen to provide us with an accurate estimation of the rotor's generated power based on its blade design, numbers and associated pitch angles. Based on the calculated effects of blade specifications on the rotor's energy harvesting efficiency such as the blade's tip and root lengths, pitch angles and foil shape, a blade optimizing stage has been designed.

Employed optimization techniques are explained in chapter 3. Due to the high amount of non-linearity among various blade designing factors and the rotor's generated power, Design of Experiments is selected to provide a model of the rotor. Accordingly, a quadratic formula succeeded in addressing both the mentioned non-linearity and also the

existing factors interactions. By taking advantage of Steepest Ascent Methodology, the optimum blade characteristics are demonstrated in the variation of the rotor blade numbers. As a result, the optimization with NACA 0012 foil profiles boosted the rotor's power capabilities up to six times compared to conventional blades.

The resultant blade described in chapter 3 has low span-wise thicknesses which make it prone to blade deformation, especially blade tip deflection, during its performance. Thus, it was necessary to investigate the blade structural behavior. Another factor that has to be kept in mind is the blade vibrations which, if not addressed carefully, can greatly decrease the rotor efficiency. Accordingly, in chapter 4, a two dimensional analysis is performed on the blade optimized foil shape to both state its hydrodynamic lift and drag coefficients characteristics and also to examine the unsteady behavior of the blade. This is a good estimation of the blade vibrational domains. Based on the *2D* results, a three dimensional calculation was conducted to calculate the startup unsteady load distribution over the upper and lower blade surfaces during the rotor's start up. Afterwards, a finite element analysis was performed to analyze the blade's tip deflection based on the *3D* load calculations. These calculations provide us with important information about the choice of material to ensure the safe performance of the blades.

5.2 Contributions

This section will discuss the main contributions of the thesis, the designed rotor performance criteria and limitations.

Based on the nature of the ocean current streams and associated available kinetic energy, the generated power from the rotor is expected to be around a watt which makes the designing of the rotor a challenge. In order to avoid the need for expensive and time consuming actual rotor testing, a rotor's *BEM* model provides us with accurate rotor power generation simulation. Considering the steady state assumption in our developed *BEM* model, the unsteady start up rotor behavior cannot be modeled through this modeling methodology. Thus, the modeling results should be disregarded during the start-up stage. To model this step, an unsteady *CFD* approach was employed to accurately estimate the rotor behavior and blade load distribution contours.

It is of note that to address limited experimental data availability regarding the NACA four series foil's hydrodynamic characteristics for Reynolds number less than 40000, the *XFOIL* package is used to calculate related lift and drag coefficients. The package calculated coefficients validation with the experimental data at $Re = 80000$ reveal that these factors are over predicted especially after the stalling phenomenon happened. Nevertheless, the lift to drag ratio follows the same trend and stays near to the experimental data which has the most significant effect on the rotor design. From modeling results, it can be concluded that the *BEM* model shows good accuracy in steady state rotor modeling.

The Design of Experiments optimization technique is selected to perform the optimization procedure. The correctness and accuracy of the proposed design is compared with the developed turbine blade element momentum theory model which is demonstrated to be in an acceptable range. It is important to mention that the two stage

optimization will not model the interaction between changing the number of blades and tip and root lengths and the 2D blade foil shape. In spite of the fact that this effect is assumed to be negligible, it is beneficial to further investigate the accuracy of this assumption through designing a one-stage optimization. This includes the whole designing factors in a single *CCD* design. In addition, the thickness allowance was limited in our design. The main reason for not allowing lower foil thicknesses was mainly due to the blade tip deflection considerations, manufacturing techniques and material choice restrictions.

With respect to the 2D *CFD* analysis, the procedure of calculating the 2D foil lift and drag factors is extracted through validating the similar calculations with Eppler 61 at the $Re = 42000$. This procedure is an alternative for the fact that there is no experimental data available for our *CFD* calculations. The methodology in this section can be improved by validating the NACA 6603 foil result with related experimental data. Nevertheless, considering the shape and the flow behavior similarity between these two foils, the results in this part are considered to be accurate. In the next step, and based on the 2D result validation, the 3D start-up calculations are considered to be the source of unsteady blade load estimations. The finite element analysis then provides us with necessary information regarding the selection of the material and manufacturing techniques to produce our designed thin blades.

Rotor design developed in this thesis is optimized to address a novel low current streams application in which the rotor's higher generated torque enables us to start energy harvesting from very low speed water regimes. Accordingly, the mechanical design of the

system is ready for manufacturing with the suggested material and manufacturing techniques. It is also ready for laboratory testing.

5.3 Future Work

The designed rotor has the ability of providing low density power for small sensing units on the seabed. However, the performance of the design is yet to be investigated experimentally. The suggested methodology can be further employed to harness energy generally from any low current streams of water or wind velocities. In order to boost the rotor generated power with the proposed method, advances in material and manufacturing technologies can push the foil thickness limitations and produce even thinner blades.

Regarding the rotor modeling and optimization sections, the accuracy of the modeling can be increased by using experimental foil lift and drag coefficients or employing more accurate software to calculate these factors. It is also beneficial to consider other classes of foils as the DoE optimization space to examine if more lift to drag ratio can be produced in mentioned Reynolds number regimes. In addition, through designing a single optimization stage which includes all the factors at once it is possible to get more precise optimization results. This can be done with the help of other gradient based optimization methods or even employing the genetic algorithm technique as well.

From the point of view of *CFD* and *FEA* simulation analysis, considering a test ready setup of the rotor, including housing and experimental set up, results in a more realistic analysis of the rotor power generation capabilities. Moreover, having wider range of

material choice and manufacturing techniques is beneficial in decreasing the amount of blade tip deflection in the *FEA* analysis.

Considering the low generated torque by this rotor, the energy loss through a gearbox will diversely affect the startup and also the whole performance of the rotor. To address this issue, a magnetic coupling approach can be suggested which will completely separate the rotor and the generator box from each other. Thus, the magnetic force will transfer the generated torque to the sealed housing. In this way, there will be no need for a gearbox and also to make the generator waterproof. Accordingly, the maintenance or any rotor modification will not affect the generator performance. One downside of this method will be more rotational resistant resulted from magnetic inertia comparing to conventional shaft connection. In the water, the oil compensating method, in which the whole housing will be filled with oil, can be used to make the pressure difference around the housing near to zero. However, this will add to the shaft rotational resistance.

Another issue that has to be further investigated is the cogging torque generated from Permanent Magnet Generators (PMG) which will cause resistance and vibrations during the start-up process of the rotor. Many methods are available to reduce this undesired torque including non-uniform stator air gap, pole shifting and sizing, stator tooth notching and skewing the generator stack [92]. However, the appropriate approach has to be selected with care to match our low cut-in speed rotor start-up torque.

In the end, the proposed rotor design in this thesis is an initial step in designing ocean current low cut-in speed rotors which are not yet fully explored. Powering low power consumption geological sensing packages deployed on the seabed is an example of this

rotor's application. Considering the maintenance cost of the battery change of such a sensing unit, the need for such a low cut-in speed rotor is further demonstrated.

References

- [1] J. M. Ferrieri, and E. T. Wiseman, *An evaluation of lifting line theory as applied to a current turbine design with model test validation*, Webb Institute, Glen Cove, NY, USA, 2011.
- [2] E. Hau, *Wind turbines fundamentals, technologies, application, economics*, 2nd edition, Springer-Verlag Berlin Heidelberg, 2006.
- [3] D. W. Wu, and R. Z. Wang, "Combined cooling, heating and power: a review," *Progress in Energy and Combustion Science*, Vol. 32, pp. 459-495, 2006.
- [4] A. H. Lefebvre, *Gas turbine combustion*, Second Edition, Edwards Brothers, Ann Arbor, MI, 1998.
- [5] J. R. Fanchi, and C. J. Fanchi, *Energy in the 21st century*, 2nd Edition, World Scientific Publishing Co. Pte. Ltd., Singapore, 2011.
- [6] J. S. Anagnostopoulos, and S. E. Papantonis, "Optimal sizing of a run-of-river small hydropower plant," *Energy Conversion and Management*, Vol. 48, pp. 2663-2670, 2007.
- [7] I. Hadjipaschalis, A. Poullikkas, and V. Efthimiou, "Overview of current and future energy storage technologies for electric power applications," *Renewable and Sustainable Energy Reviews*, Vol. 13, pp. 1513-1522, 2009.
- [8] J. H. Munro, "Industrial energy from water-mills in the European economy, 5th to 18th centuries: the limitations of power," Munich Personal RePEc Archive

(MPRA), Paper No. 11027, October 2008.

- [9] M. J. Khan, G. Bhuyan, M. T. Iqbal, and J. E. Quaicoe, "Hydrokinetic energy conversion systems and assessment of horizontal and vertical axis turbines for river and tidal applications: a technology status review," *Applied Energy*, Vol. 86, pp. 1823-1835, 2009.
- [10] R. Chini, M. Ordonez, and R. Bachmayer, "Blades optimization for an ocean current horizontal axis turbine using response surface methodology," *IEEE Oceans'11 Conference, Santander (Spain)*, pp. 1-8, Jun. 6-9, 2011.
- [11] N. Pearce, "Worldwide tidal current energy developments and opportunities for Canada's pacific coast," *International Journal of Green Energy*, Vol. 2:4, pp. 365-386, 2005.
- [12] DFO, 2009, "Assessment of tidal and wave energy conversion technologies in Canada," DFO. Canadian Science Advisory Secretariat Science Report 2009/064.
- [13] A. Cornett, 2006, "Inventory of Canada's marine renewable energy resources," Canadian Hydraulics Centre (CHC), Technical Report CHC-TR-041.
- [14] J. Falnes, and J. Lovseth, "Ocean wave energy," *Energy Policy*, Vol. 19, Issue 8, pp. 768-775, 1991.
- [15] J. Cruz, *Ocean wave energy current status and future perspectives*, Springer – Verlag Berlin Heidelberg, 2008.
- [16] Z. Yong, and S. Xiaohui, "Tidal energy: technologies and recent developments," *IEEE International Energy Conference and Exhibition (EnergyCon)*, Manama

(Bahrain), pp. 618-623, Dec. 18-22, 2010.

- [17] S. E. B. Elghali, R. Balme, and K. L. Saux, "A simulation model for the evaluation of the electrical power potential harnessed by a marine current turbine," *IEEE Journal of Oceanic Engineering*, Vol. 32, No. 4, pp. 786-797, 2007.
- [18] P. L. Fraenkel, "Tidal current energy technologies," *IBIS The International Journal of Avian Science*, Special Issue: Wind, Fire and Water: Renewable Energy and Birds, Vol. 148, Issue Supplement S1, pp. 145-151, 2006.
- [19] R. Pele, and R. M. Fujita, "Renewable energy from the ocean," *Marine Policy*, Vol. 26, pp. 471-479, 2002.
- [20] R. H. Charlier, "Forty candles for the Rance river TPP tides provide renewable and sustainable power generation," *Renewable and Sustainable Energy Reviews*, Vol. 11, pp. 2032-2057, 2007.
- [21] B. Keefer, and J. Taylor, "Resource optimization approach to tidal energy," *Canada & the World of Ocean Renewable Energy Symposium*, Victoria, BC, May 4-5, 2006.
- [22] M. S. Guney, and K. Kaygusuz, "Hydrokinetic energy conversion systems: a technology status review," *Renewable and Sustainable Energy Reviews*, Vol. 14, pp. 2996-3004, 2010.
- [23] H. Stommel, "The westward intensification of wind-driven ocean currents," *Eos, Transactions, American Geophysical Union*, Vol. 29, No. 2, pp. 202-206, 1948.
- [24] K. Bryan, "A numerical investigation of a nonlinear model of a wind-driven

- ocean," *Journal of the Atmospheric Sciences*, Vol. 20, Issue 6, pp. 594-606, 1963.
- [25] P. Chapman, "Ocean Currents," retrieved from <http://www.waterencyclopedia.com/Mi-Oc/Ocean-Currents.html#b>
 - [26] D. G. Mountain, "Direct measurements in the Labrador Current," *Journal of Geophysical Research*, Vol. 85, pp. 4097-4100, 1980.
 - [27] T. H. Reynaud, A. J. Weaver, and R. J. Greatbatch, "Summer mean circulation of the northwestern Atlantic Ocean," *Journal of Geophysical Research*, Vol. 100, No. C1, pp. 779-816, 1995.
 - [28] T. Ackermann, *Wind power in power systems*, John Wiley & Sons, Ltd, the Atrium, Southern Gate, Chichester, England, 2005.
 - [29] A. Y. Wang, and C. G. Sodini, "A Simple Energy Model for Wireless Microsensor Transceivers," *IEEE Global Telecommunications Conference, GLOBECOM'04*, Vol. 5, pp. 3205-3209, Nov. 29-Dec. 3, 2004.
 - [30] V. Raghunathan, "Energy-aware wireless microsensor networks," *IEEE Signal Processing Magazine*, Vol. 19, Issue 2, pp. 1053-5888, 2002.
 - [31] B. M. Nagai, K. Ameku, and J. N. Roy, "Performance of a 3 kW wind turbine generator with variable pitch control system," *Applied Energy*, Vol. 86, pp. 1774-1782, 2008.
 - [32] R. Vijay, *Pitch Control of Horizontal Axis Wind Turbine*, Department of Electrical Engineering, National Institute of Technology, Rourkela, 2011.
 - [33] A. C. Hansen, and C. P. Butterfield, "Aerodynamics of horizontal-axis wind

- turbines," *Annual Review of Fluid Mechanics*, Vol. 25, pp. 115-149, 1993.
- [34] M. Islam, D. S. –K. Ting, and A. Fartaj, "Aerodynamic models for Darrieus-type straight-bladed vertical axis wind turbines," *Renewable and Sustainable Energy Reviews*, Vol. 12, pp. 1087-1109, 2008.
 - [35] D. W. Wu, and R. Z. Wang, "Variable Pitch Darrieus Water Turbines," *Journal of Fluid Science and Technology*, Vol. 3, No. 3, pp. 430-438, 2008.
 - [36] U. K. Saha, and M. J. Rajkumar, "On the performance analysis of Savonius rotor with twisted blades," *Renewable Energy*, Vol. 31, pp. 1776-1788, 2006.
 - [37] K. Golecha, T. I. Eldho, and S. V. Prabhu, "Study on the interaction between two hydrokinetic Savonius turbines," *International Journal of Rotating Machinery*, Vol. 2012, pp. 1-10, 2012.
 - [38] M. N. I. Khan, M. T. Iqbal, M. Hinchey, and V. Masek, "Performance of savonius rotor as a water current turbine" *The Journal of Ocean Technology. Reviews & Papers, Maritime and Port Security*, Vol. 4, No. 2, pp. 71-83, 2009.
 - [39] P. N. Shankar, "Development of vertical axis wind turbines," *Proceeding of Indian Academy of Science*, Vol. C 2, Pt. 1, pp. 49-66, 1979.
 - [40] R. A. McAdam, G. T. Houlshby, M. L. G. Oldfield, and M. D. McCulloch, "Experimental testing of the transverse horizontal axis water turbine," *Proceeding of the 8th European Wave and Tidal Energy Conference*, Uppsala (Sweden), pp. 360-365, 2009.
 - [41] Transverse horizontal axis water turbine, retrieved from:
<http://www.eng.ox.ac.uk/tidal/research/transverse-horizontal-axis-water-turbine>

- [42] R. Susan-resiga, S. Muntean, S. Bernad, T. Frunza, and D. Balint, "Thin hydrofoil cascade design and numerical flow analysis part I - design," Proceeding of the Romanian academy, Series A, Vol. 7, No. 2/2006, pp. 000-000, 2006.
- [43] A. H. Techet, J. J. Allen, and A. J. Smits, "Piezoelectric eels for energy harvesting in the ocean," Proceeding of the twelfth International Offshore and Polar Engineering Conference, Kitakyushu (Japan), May 26-31, 2002.
- [44] M. M. Bernitsas, K. Raghavan, Y. Ben-Simon, and E. M. H. Garcia, "VIVACE (Vortex Induced Vibration Aquatic Clean Energy) a new concept in generation of clean and renewable energy from fluid flow," Journal of Offshore Mechanics and Arctic Engineering, Vol. 130, pp. (041101) 1-15, 2008.
- [45] Md. J. Alam, and M. T. Iqbal, "A low cut-in speed marine current turbine," The Journal of Ocean Technology. Reviews & Papers, Safety@Sea, Vol. 5, No. 4, pp. 49-61, 2010.
- [46] J. Falnes, and J. Lovseth, "Horizontal axis tidal current turbine: numerical and experimental investigation," Owemes 2006, Civitavecchia (Italy), Apr. 20-22, 2006.
- [47] M. O. L. Hansen, *Aerodynamics of wind turbines*, 2nd Edition, Earthscan, London, Sterling, VA, 2008.
- [48] H. A. Madsen, R. Mikkelsen, S. Oye, C. Bak, and J. Johansen, "A detailed investigation of the Blade Element Momentum (BEM) model based on analytical and numerical results and proposal for modifications of the BEM model,"

Journal of Physics: Conference Series 75, 012016, 2007.

- [49] M. M. Duquette, and K. D. Visser, "Numerical implications of solidity and blade number on rotor performance of horizontal-axis wind turbines," *Journal of Solar Energy Engineering*, Vol. 125, pp. 425-432, 2003.
- [50] K. Stewartson, "A note on lifting line theory," *Quarterly Journal of Mechanics and Applied Mathematics*, Vol. XIII, Pt. 1, 1960.
- [51] G. B. Eke, and J. I. Onyewudiala, "Optimization of wind turbine blades using genetic algorithm," *Global Journal of Research in Engineering*, Vol. 10, Issue 7, pp. 22-26, 2002.
- [52] T. Diveus, P. Sebastian, D. Bernard, and J. R. Puiggali, "Horizontal axis wind turbine systems: Optimization using genetic algorithms," *Wind Energy*, Vol. 4, pp. 151-171, 2001.
- [53] K. Maalawi, "Special issues on design optimization of wind turbine structures," Ibrahim Al-Bahadly (Ed.), *Wind Turbines*, pp. 3-24, InTech, April 2011.
- [54] S. Pierret, and C. Hirsch "An integrated optimization system for Turbomachinery blade shape design," presented at the RTO AVT Symposium on "reduction of military vehicle acquisition time and cost through advanced modelling and virtual simulation", Paris (France), Apr. 22-25, 2002.
- [55] J. Reuther, A. Jameson, J. Farmer, L. Martinelli, and D. Saunders, "Aerodynamic shape optimization of complex aircraft configurations via an adjoint formulation," 34th Aerospace Sciences meeting and exhibit, AIAA, Reno, NV, Jan. 15-18, 1996.

- [56] F. Neri, and V. Tirronen, "On memetic differential evolution frameworks: a study of advantages and limitations in hybridization, IEEE World Congress on Computational Intelligence, CEC 2008, pp. 2135-2142, Hong Kong, Sep. 23, 2008.
- [57] A. A. Giunta, R. Narducci, and S. Burgee, "Variable complexity response surface aerodynamic design of an HSCT wing," Computational Mechanics, Vol. 18, No. 2, pp. 112-126, 1996.
- [58] K. C. Giannakoglou, "Design of optimal aerodynamic shapes using stochastic optimization methods and computational intelligence," Progress in Aerospace Sciences, Vol. 38, pp. 43-76, 2002.
- [59] N. Sezer-Uzol, and L. N. Long, "3-D time-accurate CFD simulations of wind turbine rotor flow fields," 44th AIAA Aerospace Sciences Meeting and Exhibit, Reno, Nevada, Jan. 9-12, 2006.
- [60] E. Ferrer, and X. Munduate, "Wind turbine blade tip comparison using CFD", Journal of Physics: Conference Series 75, 012005, 2007.
- [61] L. J. Vermeer, J. N. Sorensen, and A. Crespo, "Wind turbine wake aerodynamics," Progress in Aerospace Sciences, Vol. 39, pp. 467-510, 2003.
- [62] A. L. Pape, and J. Lecanu, "3D Navier-Stokes computations of a stall-regulated wind turbine," Wind Energy, Vol. 7, pp. 309-324, 2004.
- [63] B. M. Nagai, K. Ameku, and J. N. Roy, "Laminar separation bubble on an Eppler 61 foil," International Journal for Numerical Methods in Fluids, Vol. 64, pp. 627-652, 2010.

- [64] Z. L. Mahri, and M. S. Rouabah, "Calculation of dynamic stresses using finite element method and prediction of failure for wind turbine rotor," WSEAS transaction on Applied and Theoretical Mechanics, Vol. 3, Issue 1, pp. 28-41, 2008.
- [65] N. M. El Chazly, "Static and dynamic analysis of wind turbine blades using the finite element method," Renewable Energy, Vol. 3, No. 6/7, pp. 705-724, 1993.
- [66] M. E. Bechly, and P. D. Clausen, "Structural design of a composite wind turbine blade using finite element analysis," Computers & Structures, Vol. 63, No. 3, pp. 639-646, 1997.
- [67] F. M. Jensen, B. G. Falzon, J. Ankersen, and H. Stang, "Structural testing and numerical simulation of a 34 m composite wind turbine blade," Composite Structures, Vol. 76, pp. 52-61, 2006.
- [68] R. Lanzafame, and M. Messina, "Fluid dynamics wind turbine design: Critical analysis, optimization and application of BEM theory," Renewable Energy, Vol. 32, pp. 2291-2305, 2007.
- [69] S. Duran, *Computer-aided design of horizontal-axis wind turbine blades*, Middle east technical university, Ankara, Turkey, 2005.
- [70] J. O. Ajedegba, *Effects of blade configuration on flow distribution and power output of a zephyr vertical axis wind turbine*, University of Ontario institute of technology, Oshawa, Ontario, Canada, 2008.
- [71] L. Lazauskas, "AIROIL: NACA 0015, DATA: Lift Coefficients," retrieved from <http://www.cyberiad.net/library/airfoils/foildata/n0015c1.htm>

- [72] L. Lazauskas, "AIROIL: NACA 0015, DATA: Drag Coefficients," retrieved from
<http://www.cyberiad.net/library/airfoils/foildata/n0015cd.htm>
- [73] P. J. Philips, R. A. East, and N. H. Pratt, "An unsteady lifting line theory of flapping wings with application to the forward flight of birds," *Journal of Fluid Mechanics*, Vol. 112, pp. 97-125, 1980.
- [74] M. Drela, "XFOIL: An analysis and design system for low Reynolds number airfoils," *Low Reynolds Number Aerodynamics*, Springer-Verlag, Lec. Notes in Eng.54, 1989.
- [75] W. M. J. Batten, A. S. Bahaj, A. F. Molland, and J. R. Chaplin, "Hydrodynamics of marine current turbines," *Renewable Energy*, Vol. 31, pp. 249-256, 2006.
- [76] A. S. Bahaj, W. M. J. Batten, and G. McCann, "Experimental verifications of numerical predictions for the hydrodynamic performance of horizontal axis marine current turbines," *Renewable Energy*, Vol. 32, pp. 2479-2490, 2007.
- [77] A. S. Bahaj, A. F. Molland, J. R. Chaplina, and W. M. J. Battena, "Power and thrust measurements of marine current turbines under various hydrodynamic flow conditions in a cavitation tunnel and a towing tank," *Renewable Energy*, Vol. 32, pp. 407-426, 2007.
- [78] D. C. Montgomery, *Design and Analysis of Experiments*, 5th edition, John Wiley & Sons, Inc., NY, USA, 2001.
- [79] V. Czitrom, "One-factor-at-a-time versus designed experiments," *The American Statistician*, Vol. 53, No. 2, pp. 126-131, 1999.

- [80] L. Lye, Class lecture for Engr. 9516: Similitude, modelling, and data analysis, St. John's Campus, Memorial University of Newfoundland, St. John's, NL, Canada, 2011.
- [81] C. B. Linfield and P. M. Berthouex, *Statistics for environmental engineers*, Chapter 43, 2nd edition, CRC press, USA, 2002.
- [82] P. Fu, and M. Farzaneh, "A CFD approach for modeling the rime-ice accretion process on a horizontal-axis wind turbine," *Journal of Wind engineering and Industrial Aerodynamics*, Vol. 98, pp. 181-188, 2010.
- [83] T. J. Mueller, to be presented at the RTO AVT/VKI special course: Development and operation of UAVs for military and civil applications, VKI, Belgium, September 13-17, 1999.
- [84] S. B. Savaliya, S. P. Kumar and S. Mittal, "Laminar separation bubble on an Eppler 61 airfoil," *International Journal for Numerical Methods in Fluids*, Vol. 64, pp. 627-652, 2010.
- [85] S. Yarusevych, P. Sullivan and G. Kawall, "On vortex shedding from an airfoil in low-Reynolds-number flows," *Journal of Fluid Mechanics*, Vol. 632, pp. 245-271, 2009.
- [86] F. Wing, L. Bai, J. Fletcher, J. Whiteford, and D. Cullen, "Development of small domestic wind turbine with scoop and prediction of its annual power output," *Renewable Energy*, Vol. 33, pp. 1637-1651, 2008.
- [87] F. Wing, L. Bai, J. Fletcher, J. Whiteford, and D. Cullen, "The methodology for aerodynamic study on a small domestic wind turbine with scoop," *Journal of*

Wind Engineering and Industrial Aerodynamics, Vol. 96, pp. 1-24, 2008.

- [88] DuraForm PA & GF plastic for use with all SLS systems, retrieved from:
<http://www.bastech.com/sls/materials/duraformpadatasheet.asp>
- [89] E. A. C. Johnson, P. G. Young, "On the use of a patient-specific rapid-prototyped model to simulate the response of the human head to impact and comparison with analytical and finite element models, *Journal of Biomechanics*, Vol. 38, pp. 39-45, 2005.
- [90] Fortus FDM Thermoplastic, retrieved from:
<http://www.bastech.com/sls/materials/duraformpadatasheet.asp>
- [91] SolidWorks Flow Simulation 2010 Technical Reference.
- [92] E. Muljadi and L. Green, "Cogging Torque Reduction in a Permanent Magnet Wind Turbine Generator," 21st American Society of Mechanical Engineers Wind Energy Symposium, Jan. 14-17, 2002.

Appendices

Appendix A:

Clarifications on Blade Element Momentum Theory Formulation

Regarding the ideal rotor assumptions, the velocity decrease from V_0 to u_1 is reformed to thrust T and shaft power P components. The thrust which is resulted from pressure drop can be formulated as equation (A.1). The flow in the first control volume explained in Fig 2.7 is non-rotating, incompressible and frictionless. Thus it is possible to apply the Bernoulli equation for the control volume except from the regions near the rotor (both in upstream and downstream) where the sudden pressure drop is happening, see equations (A.2) and (A.3) [47].

$$T = \Delta p A \quad \text{A.1}$$

$$p_0 + \frac{1}{2} \rho V_0^2 = p + \frac{1}{2} \rho u^2 \quad \text{A.2}$$

$$\Delta p = \frac{1}{2} \rho (V_0^2 - u_1^2) \quad \text{A.3}$$

By applying axial momentum equation on the same control volume, the equation (A.4) and (A.5) are derived. The first and last terms in the axial momentum equation are zero while the flow is assumed to be stationary and the pressures in the first and last plates are equal to the same atmospheric pressure on an equal area. Applying the

conservation of mass the \dot{m}_{side} can be formulated as equation (A.6). Considering equations (A.4), (A.6) and (A.7), the thrust can be expressed by equation (A.8) [47].

$$\rho u_1^2 A_1 + \rho V_0^2 (A_{cv} - A_1) + \dot{m}_{side} V_0 - \rho V_0^2 A_{cv} = -T \quad A.4$$

$$\rho A_1 u_1 + \rho (A_{cv} - A_1) V_0 + \dot{m}_{side} = \rho A_{cv} V_0 \quad A.5$$

$$\dot{m}_{side} = \rho A_1 (V_0 - u_1) \quad A.6$$

$$\dot{m} = \rho u A = \rho u_1 A_1 \quad A.7$$

$$T = \rho u A (V_0 - u_1) = \dot{m} (V_0 - u_1) \quad A.8$$

Similarly the shaft power can be formulated by applying the integral energy equation on the second control volume shown in the Fig. 2.7, see equations (A.9) and (A.10). Combining equations (A.1) and (A.3), the velocity in the rotor plane can be shown as equation (A.11). Combining the axial induction factor definition, see equation (2.4), and equation (A.11), u_1 can be exhibited as equation (A.12). As a result, the shaft power and thrust can be shown as equations (A.13) and (A.14). The power coefficient C_p defined as the actual power divided by available kinetic power from the flow, see equation (A.15). Using the equation (A.13) and combine it with equation (A.15), equation (A.16) is resulted. A comprehensive description of BEM modeling formulations can be found from [47].

$$P = \dot{m} \left(\frac{1}{2} V_0^2 + \frac{p_0}{\rho} - \frac{1}{2} u_1^2 - \frac{p_0}{\rho} \right) \quad A.9$$

$$P = \frac{1}{2}\rho uA(V_0^2 - u_1^2) \quad \text{A.10}$$

$$u = \frac{1}{2}(V_0 + u_1) \quad \text{A.11}$$

$$u_1 = (1 - 2a)V_0 \quad \text{A.12}$$

$$P = 2\rho V_0^3 a(1 - a)^2 A \quad \text{A.13}$$

$$T = 2\rho V_0^2 a(1 - a)A \quad \text{A.14}$$

$$C_p = \frac{P}{\frac{1}{2}\rho V_0^3 A} \quad \text{A.15}$$

$$C_p = 4a(1 - a)^2 \quad \text{A.16}$$

Appendix B:

Introduction to Design of Experiments

All the DOE analyses are based on ANOVA which tests the statistical significance and the regression analysis which produces the prediction model. A Central Composite Design (CCD) is forming by adding a center point and five axial points to the main 2^k factorial designs. For more than two factor levels, the ANOVA analysis will be applied. The equations (B.1) to (B.4) explain the basic ANOVA analysis further. In equation (B.1), μ , τ_i and ε_{ij} stand for an overall mean, i th treatment effect and experimental error respectively. The total variability is represented by the “Sum of Squares” which reflects the differences in treatment means; see equations (B.2) and (B.3) where $i = 1, 2, \dots, a$ indicates the number of factor levels or treatments, $j = 1, 2, \dots, n$ represents the number of replicates, \bar{Y} and \bar{Y}_i are the overall and treatment means and Y and SS_E stand for factors’ response and related error’s sum of squares. The large value for $SS_{Treatment}$ means large differences between treatment means and accordingly a small value will demonstrate no difference between treatment means. The statistical hypothesis is demonstrated in equation (B.5).

$$Y_{ij} = \mu + \tau_i + \varepsilon_{ij}, \begin{cases} i = 1, 2, \dots, a \\ j = 1, 2, 3, \dots, n \end{cases} \quad (B.1)$$

$$SS_T = \sum_{i=1}^a \sum_{j=1}^n (Y_{ij} - \bar{Y})^2 = n \sum_{i=1}^a (\bar{Y}_i - \bar{Y})^2 + \sum_{i=1}^a \sum_{j=1}^n (Y_{ij} - \bar{Y}_i)^2 \quad (B.2)$$

$$\bar{y} = \frac{1}{n} \sum_{i=1}^n y_i \quad (\text{B.3})$$

$$SS_T = SS_{Treatments} + SS_E \quad (\text{B.4})$$

$$\begin{aligned} H_0: \mu_1 = \mu_2 = \dots = \mu_a \\ H_1 = \text{At least one mean is different} \end{aligned} \quad (\text{B.5})$$

The sums of squares cannot be directly used to handle the hypothesis of equal means, thus, the “Mean Square” will be utilized for decision making purposes. Equations (B.6) and (B.7) demonstrate that the mean square equates to sum of squares divided by its degree of freedom (df). The F-test (B.8) should satisfy the (B.9) comparison and then the factors’ effect will be significant at the 5% significance level [80].

$$MS_T = \frac{SS_{Treatments}}{a - 1}, MS_E = \frac{SS_E}{a(n - 1)} \quad (\text{B.6})$$

$$df_{Total} = df_{Treatments} + df_{Error} \quad (\text{B.7})$$

$$F_0 = \frac{MS_{Treatments}}{MS_E} \quad (\text{B.8})$$

$$F_0 > F_{0.05, a-1, a(n-1)} \quad (\text{B.9})$$

After stating the statistical significance of the model, it is time to use a regression model and fit it to the associated response surface. Accordingly, the related regression model is stated as (B.10) where Y is the response, β_i and β_{ij} are the coefficients that have to be determined and X_i are representatives of the design factors. The response surface and related contour plot of the model is exhibited in Figs. B.1 and B.2.

$$Y = \beta_0 + \sum \beta_i X_i + \sum \sum \beta_{ij} X_i X_j + \varepsilon \quad (\text{B.10})$$

In case the simpler full factorial design was unable to model the design factors and response behavior, due to having discrete values of A , B and C with mentioned constraints, a faced Centered Composite Design (*CCD*), with one center point is selected for analyzing the power response surface [78], [80]. The reason of placing the one center point is to see the level that the quadratic model can fit to the data. The general form of the nonlinear quadratic model is presented in (B.11). It has to be noted that the third order interactions are omitted from the quadratic model mainly due to their lower effect on response surface and also to keep the model simple [78].

$$Y = \beta_0 + \sum \beta_i X_i + \sum \sum \beta_{ij} X_i X_j + \sum \beta_{ii} X_i^2 + \varepsilon \quad (\text{B.11})$$

As it is seen in equation (B.10), the linear, interaction and quadratic terms are included in the final system model. Generally, most non-linear systems with ‘smooth’ response surface can be modeled accurately with a quadratic equation, see Figs. B.3 and B.4. When the rotor generated power response surface is modeled with either *FFD* or *CCD* designs, it is possible to optimize the blade geometry and shape based on the power contour behaviors.

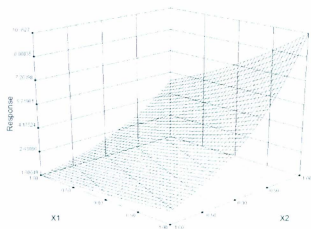


Fig. B.1 X_1 vs. X_2 response surface plot (FFD)

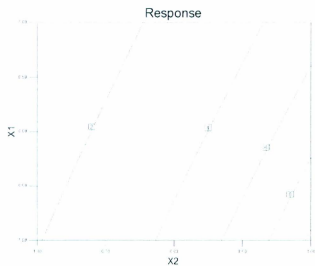


Fig. B.2 X_1 vs. X_2 contour plot

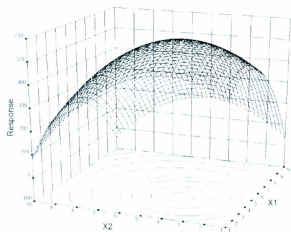


Fig. B.3 X_1 vs. X_2 response surface plot (CCD)

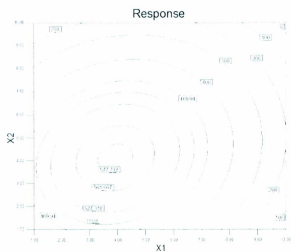


Fig. B.4 X_1 vs. X_2 contour plot

Appendix C:

CFD Governing Equations

Flow Simulation solves Navier-Stokes equations and is able to predict both laminar and turbulent flows. This package is also capable of transmission between two laminar and turbulent flows during the simulations. This is crucial capability for our low Reynolds number flow simulations. In turbulent flow, the turbulent kinetic energy and its dissipation rate are addressed by $k - \varepsilon$ model.

Let Ω be the angular velocity about an axis which passes through the origin and u and ρ be the fluid velocity and density. The spatial and temporal coordinates are represented by x and t . Here, τ_{ik} , Q_H , q_i , h and S_i are the viscous shear stress, heat source/sink, the diffusive heat flux, the thermal enthalpy and an external force caused by a mass distribution per mass [91].

$$\frac{\partial \rho}{\partial t} + \frac{\partial}{\partial x_i} (\rho u_i) = 0 \quad \text{C.1}$$

$$\frac{\partial \rho u_i}{\partial t} + \frac{\partial}{\partial x_j} (\rho u_i u_j) + \frac{\partial p}{\partial x_i} = \frac{\partial}{\partial x_i} (\tau_{ij} + \tau_{ij}^R) + S_i i = 1, 2, 3 \quad \text{C.2}$$

$$\frac{\partial \rho H}{\partial t} + \frac{\partial \rho u_i H}{\partial x_i} = \frac{\partial}{\partial x_i} (u_j (\tau_{ij} + \tau_{ij}^R) + q_i) + \frac{\partial p}{\partial t} - \tau_{ij}^R \frac{\partial u_i}{\partial x_j} + \rho \varepsilon + S_i u_i + Q_H \quad \text{C.3}$$

$$H = h + \frac{u^2}{2}$$

The viscous shear stress for Newtonian fluids and the Reynolds-stress tensor are defined as below equations where δ_{ij} , μ , μ_t , ε , f_μ and k stand for Kronecker delta function (if $i = j$ then $\delta_{ii} = 1$ and otherwise $\delta_{ij} = 0$), dynamic viscosity coefficient, turbulent eddy viscosity coefficient, turbulent dissipation, turbulent viscosity factor and turbulent kinetic energy respectively [91].

$$\tau_{ij} = \mu \left(\frac{\partial u_i}{\partial x_j} + \frac{\partial u_j}{\partial x_i} - \frac{2}{3} \delta_{ij} \frac{\partial u_k}{\partial x_k} \right) \quad \text{C.4}$$

$$\tau_{ij}^R = \mu_t \left(\frac{\partial u_i}{\partial x_j} + \frac{\partial u_j}{\partial x_i} - \frac{2}{3} \delta_{ij} \frac{\partial u_k}{\partial x_k} \right) - \frac{2}{3} \rho k \delta_{ij} \quad \text{C.5}$$

$$\mu_t = f_\mu \frac{c_\mu \rho k^2}{\varepsilon} \quad \text{C.6}$$

$$f_\mu = \left[1 - e^{(-0.025 R_y)} \right]^2 \cdot \left(1 + \frac{20.5}{R_T} \right) \quad \text{C.7}$$

$$R_T = \frac{\rho k^2}{\mu \varepsilon} \quad \text{C.8}$$

$$R_y = \frac{\rho \sqrt{k} y}{\mu} \quad \text{C.9}$$

where y is the distance from the wall. Turbulent kinetic energy and dissipation equations are demonstrated from equations C.10 and C.11.

$$\frac{\partial \rho k}{\partial t} + \frac{\partial}{\partial x_i} (\rho u_i k) = \frac{\partial}{\partial x_i} \left(\left(\mu + \frac{\mu_t}{\sigma_k} \right) \frac{\partial k}{\partial x_i} \right) + S_k \quad \text{C.10}$$

$$\frac{\partial \rho \varepsilon}{\partial t} + \frac{\partial}{\partial x_i} (\rho u_i \varepsilon) = \frac{\partial}{\partial x_i} \left(\left(\mu + \frac{\mu_t}{\sigma_\varepsilon} \right) \frac{\partial \varepsilon}{\partial x_i} \right) + S_\varepsilon \quad \text{C.11}$$

$$S_k = \tau_{ij}^R \frac{\partial u_i}{\partial x_j} - \rho \varepsilon + \mu_t P_B \quad \text{C.12}$$

$$S_\varepsilon = C_{\varepsilon 1} \frac{\varepsilon}{k} \left(f_1 \mu_{ij}^R \frac{\partial u_i}{\partial x_j} + \mu_t C_B P_B \right) - C_{\varepsilon 2} f_2 \frac{\rho \varepsilon^2}{k} \quad \text{C.13}$$

$$P_B = - \frac{g_i}{\sigma_B} \frac{1}{\rho} \frac{\partial \rho}{\partial x_i} \quad \text{C.14}$$

where P_B and g_i stand for buoyancy forces' generated turbulence and component of gravitational acceleration in the direction of x_i . The constants $\sigma_B = 0.9$ and $C_\mu = 0.09$, $C_{\varepsilon 1} = 1.44$, $C_{\varepsilon 2} = 1.92$, $\sigma_k = 1$ and $\sigma_\varepsilon = 1.3$ are specified empirically and C_B is a function defined as,

$$C_B = \begin{cases} 1 & \text{if } P_B > 0 \\ 0 & \text{if } P_B \leq 0 \end{cases} \quad \text{C.15}$$

$$f_1 = 1 + \left(\frac{0.05}{I_\mu} \right)^3, f_2 = 1 - e^{(-R_T^2)} \quad \text{C.16}$$

$$q_i = \left(\frac{\mu}{\rho_F} + \frac{\mu_t}{\sigma_\varepsilon} \right) \frac{\partial h}{\partial x_i}, i = 1, 2, 3 \quad \text{C.17}$$

Here the Lewis number $Le = 1$ and $\sigma_\varepsilon = 0.9$. Pr and h are the Prandtl number and thermal enthalpy. These formulas can be used for both laminar and turbulent flows and also the transition between these two flows. For laminar flows the k and μ_t are zero [91].



